Searches for neutral Higgs bosons in e^+e^- collisions from $\sqrt{s} = 191.6$ to 201.7 GeV

J. Abdallah, P. Abreu, W. Adam, P. Adzic, T. Albrecht, T. Alderweireld, R. Alemany-Fernandez, T. Allmendinger, P P. Allport, S. Almehed, et al.

EUROPEAN ORGANIZATION FOR NUCLEAR RESEARCH

CERN–EP-Final

16-November-2001

Searches for neutral Higgs bosons in e^+e^- collisions from $\sqrt{s} = 191.6$ to 201.7 GeV

DELPHI Collaboration

Abstract

Neutral Higgs bosons of the Standard Model (SM) and the Minimal Supersymmetric Standard Model (MSSM) were searched for in the data collected in 1999 by the DELPHI experiment at centre-of-mass energies between 191.6 and 201.7 GeV with a total integrated luminosity of 228 pb^{-1}. These analyses, in combination with our results at lower energies, set 95% confidence level lower mass bounds on the Standard Model Higgs boson (107.3 GeV/c^2) and on the lightest neutral scalar (85.9 GeV/c^2) and neutral pseudoscalar (86.5 GeV/c^2) Higgs bosons in representative scans of the MSSM parameter space. An extended scan of the MSSM parameter space was also performed to test the robustness of these limits.

(To be submitted to Eur.Phys.J.C)

J.Abdallah[23], P.Abreu[21], W.Adam[48], P.Adzic[11], T.Albrecht[16], T.Alderweireld[2], R.Alemany-Fernandez[8], T.Allmendinger[16], P.P.Allport[22], S.Almehed[24], U.Amaldi[27], N.Amapane[43], S.Amato[45], E.Anashkin[34], A.Andreazza[26], S.Andringa[21], N.Anjos[21], P.Antilogus[25], W-D.Apel[16], Y.Arnoud[13], S.Ask[24], B.Asman[42], J.E.Augustin[23], A.Augustinus[8], P.Baillon[8], A.Ballestrero[43], P.Bambade[19], R.Barbier[25], D.Bardin[15], G.Barker[16], A.Baroncelli[37], M.Battaglia[8], M.Baubillier[23], K-H.Becks[50], M.Begalli[6], A.Behrmann[50], T.Bellunato[8], N.Benekos[30], A.Benvenuti[5], C.Berat[13], M.Berggren[23], L.Berntzon[42], D.Bertrand[2], M.Besancon[38], N.Besson[38], D.Bloch[9], M.Blom[29], M.Bonesini[27], M.Boonekamp[38], P.S.L.Booth[22], G.Borisov[8,20], O.Botner[46], B.Bouquet[19], T.J.V.Bowcock[22], I.Boyko[15], M.Bracko[41], R.Brenner[46], E.Brodet[33], J.Brodzicka[17], P.Bruckman[17], J.M.Brunet[7], L.Bugge[31], P.Buschmann[50], M.Calvi[27], T.Camporesi[8], V.Canale[36], F.Carena[8], C.Carimalo[23], N.Castro[21], F.Cavallo[5], M.Chapkin[40], Ph.Charpentier[8], P.Checchia[34], R.Chierici[8], P.Chliapnikov[40], S.U.Chung[8], K.Cieslik[17], P.Collins[8], R.Contri[12], G.Cosme[19], F.Cossutti[44], M.J.Costa[47], B.Crawley[1], D.Crennell[35], J.Cuevas[32], J.D'Hondt[2], J.Dalmau[42], T.da Silva[45], W.Da Silva[23], G.Della Ricca[44], A.De Angelis[44], W.De Boer[16], C.De Clercq[2], B.De Lotto[44], N.De Maria[43], A.De Min[34], L.de Paula[45], L.Di Ciaccio[36], A.Di Simone[37], K.Doroba[49], J.Drees[50], M.Dris[30], G.Eigen[4], T.Ekelof[46], M.Ellert[46], M.Elsing[8], M.C.Espirito Santo[8], G.Fanourakis[11], D.Fassouliotis[11], M.Feindt[16], J.Fernandez[39], A.Ferrer[47], F.Ferro[12], U.Flagmeyer[50], H.Foeth[8], E.Fokitis[30], F.Fulda-Quenzer[19], J.Fuster[47], M.Gandelman[45], C.Garcia[47], Ph.Gavillet[8], E.Gazis[30], D.Gele[9], T.Geralis[11], R.Gokieli[8,49], B.Golob[41], G.Gomez-Ceballos[39], P.Goncalves[21], E.Graziani[37], G.Grosdidier[19], K.Grzelak[49], J.Guy[35], C.Haag[16], F.Hahn[8], S.Hahn[50], A.Hallgren[46], K.Hamacher[50], K.Hamilton[33], J.Hansen[31], S.Haug[31], F.Hauler[16], V.Hedberg[24], M.Hennecke[16], H.Herr[8], S-O.Holmgren[42], P.J.Holt[33], M.A.Houlden[22], K.Hultqvist[42], J.N.Jackson[22], P.Jalocha[17], Ch.Jarlskog[24], G.Jarlskog[24], P.Jarry[38], D.Jeans[33], E.K.Johansson[42], P.D.Johansson[42], P.Jonsson[25], C.Joram[8], L.Jungermann[16], F.Kapusta[23], S.Katsanevas[25], E.Katsoufis[30], R.Keranen[16], G.Kernel[41], B.P.Kersevan[8,41], A.Kiiskinen[14], B.T.King[22], N.J.Kjaer[8], P.Kluit[29], P.Kokkinias[11], C.Kourkoumelis[3], O.Kouznetsov[15], Z.Krumstein[15], M.Kucharczyk[17], J.Kurowska[49], B.Laforge[23], J.Lamsa[1], G.Leder[48], F.Ledroit[13], L.Leinonen[42], R.Leitner[28], J.Lemonne[2], G.Lenzen[50], V.Lepeltier[19], T.Lesiak[17], W.Liebig[50], D.Liko[8,48], A.Lipniacka[42], J.H.Lopes[45], J.M.Lopez[32], D.Loukas[11], P.Lutz[38], L.Lyons[33], J.MacNaughton[48], A.Malek[50], S.Maltezos[30], F.Mandl[48], J.Marco[39], R.Marco[39], B.Marechal[45], M.Margoni[34], J-C.Marin[8], C.Mariotti[8], A.Markou[11], C.Martinez-Rivero[39], J.Masik[28], N.Mastroyiannopoulos[11], F.Matorras[39], C.Matteuzzi[27], F.Mazzucato[34], M.Mazzucato[34], R.Mc Nulty[22], C.Meroni[26], W.T.Meyer[1], E.Migliore[43], W.Mitaroff[48], U.Mjoernmark[24], T.Moa[42], M.Moch[16], K.Moenig[8,10], R.Monge[12], J.Montenegro[29], D.Moraes[45], S.Moreno[21], P.Morettini[12], U.Mueller[50], K.Muenich[50], M.Mulders[29], L.Mundim[6], W.Murray[35], B.Muryn[18], G.Myatt[33], T.Myklebust[31], M.Nassiakou[11], F.Navarria[5], K.Nawrocki[49], S.Nemecek[28], R.Nicolaidou[38], P.Niezurawski[49], M.Nikolenko[15,9], A.Nygren[24], A.Oblakowska-Mucha[18], V.Obraztsov[40], A.Olshevski[15], A.Onofre[21], R.Orava[14], K.Osterberg[8], A.Ouraou[38], A.Oyanguren[47], M.Paganoni[27], S.Paiano[5], J.P.Palacios[22], H.Palka[17], Th.D.Papadopoulou[30], L.Pape[8], C.Parkes[22], F.Parodi[12], U.Parzefall[22], A.Passeri[37], O.Passon[50], L.Peralta[21], V.Perepelitsa[47], A.Perrotta[5], A.Petrolini[12], J.Piedra[39], L.Pieri[37], F.Pierre[38], M.Pimenta[21], E.Piotto[8], T.Podobnik[41], V.Poireau[38], M.E.Pol[6], G.Polok[17], P.Poropat[44], V.Pozdniakov[15], P.Privitera[36], N.Pukhaeva[2,15], A.Pullia[27], J.Rames[28], L.Ramler[16], A.Read[31], P.Rebecchi[8], J.Rehn[16], D.Reid[29], R.Reinhardt[50], P.Renton[33], F.Richard[19], J.Ridky[28], I.Ripp-Baudot[9], D.Rodriguez[39], A.Romero[43], P.Ronchese[34], E.Rosenberg[1], P.Roudeau[19], T.Rovelli[5], V.Ruhlmann-Kleider[38], D.Ryabtchikov[40], A.Sadovsky[15], L.Salmi[14], J.Salt[47], A.Savoy-Navarro[23], C.Schwanda[48], B.Schwering[50], U.Schwickerath[8], A.Segar[33], R.Sekulin[35], M.Siebel[50], A.Sisakian[15], G.Smadja[25], O.Smirnova[24], A.Sokolov[40], A.Sopczak[20], R.Sosnowski[49], T.Spassov[8], M.Stanitzki[16], A.Stocchi[19], J.Strauss[48], B.Stugu[4], M.Szczekowski[49], M.Szeptycka[49], T.Szumlak[18], T.Tabarelli[27], A.C.Taffard[22], F.Tegenfeldt[46], F.Terranova[27], J.Timmermans[29], N.Tinti[5], L.Tkatchev[15], M.Tobin[22], S.Todorovova[8], B.Tome[21], A.Tonazzo[27], P.Tortosa[47], P.Travnicek[28], D.Treille[8], G.Tristram[7], M.Trochimczuk[49], C.Troncon[26], I.A.Tyapkin[15], P.Tyapkin[15], S.Tzamarias[11], O.Ullaland[8], V.Uvarov[40], G.Valenti[5], P.Van Dam[29], J.Van Eldik[8], A.Van Lysebetten[2], N.van Remortel[2], I.Van Vulpen[29], G.Vegni[26], F.Veloso[21], W.Venus[35], F.Verbeure[2], P.Verdier[25], V.Verzi[36], D.Vilanova[38], L.Vitale[44],

V.Vrba[28], H.Wahlen[50], A.J.Washbrook[22], C.Weiser[8], D.Wicke[8], J.Wickens[2], G.Wilkinson[33], M.Winter[9], M.Witek[17], O.Yushchenko[40], A.Zalewska[17], P.Zalewski[49], D.Zavrtanik[41], N.I.Zimin[15], A.Zintchenko[15], Ph.Zoller[9], M.Zupan[11]

[1]Department of Physics and Astronomy, Iowa State University, Ames IA 50011-3160, USA
[2]Physics Department, Universiteit Antwerpen, Universiteitsplein 1, B-2610 Antwerpen, Belgium
and IIHE, ULB-VUB, Pleinlaan 2, B-1050 Brussels, Belgium
and Faculté des Sciences, Univ. de l'Etat Mons, Av. Maistriau 19, B-7000 Mons, Belgium
[3]Physics Laboratory, University of Athens, Solonos Str. 104, GR-10680 Athens, Greece
[4]Department of Physics, University of Bergen, Allégaten 55, NO-5007 Bergen, Norway
[5]Dipartimento di Fisica, Università di Bologna and INFN, Via Irnerio 46, IT-40126 Bologna, Italy
[6]Centro Brasileiro de Pesquisas Físicas, rua Xavier Sigaud 150, BR-22290 Rio de Janeiro, Brazil
and Depto. de Física, Pont. Univ. Católica, C.P. 38071 BR-22453 Rio de Janeiro, Brazil
and Inst. de Física, Univ. Estadual do Rio de Janeiro, rua São Francisco Xavier 524, Rio de Janeiro, Brazil
[7]Collège de France, Lab. de Physique Corpusculaire, IN2P3-CNRS, FR-75231 Paris Cedex 05, France
[8]CERN, CH-1211 Geneva 23, Switzerland
[9]Institut de Recherches Subatomiques, IN2P3 - CNRS/ULP - BP20, FR-67037 Strasbourg Cedex, France
[10]Now at DESY-Zeuthen, Platanenallee 6, D-15735 Zeuthen, Germany
[11]Institute of Nuclear Physics, N.C.S.R. Demokritos, P.O. Box 60228, GR-15310 Athens, Greece
[12]Dipartimento di Fisica, Università di Genova and INFN, Via Dodecaneso 33, IT-16146 Genova, Italy
[13]Institut des Sciences Nucléaires, IN2P3-CNRS, Université de Grenoble 1, FR-38026 Grenoble Cedex, France
[14]Helsinki Institute of Physics, HIP, P.O. Box 9, FI-00014 Helsinki, Finland
[15]Joint Institute for Nuclear Research, Dubna, Head Post Office, P.O. Box 79, RU-101 000 Moscow, Russian Federation
[16]Institut für Experimentelle Kernphysik, Universität Karlsruhe, Postfach 6980, DE-76128 Karlsruhe, Germany
[17]Institute of Nuclear Physics,Ul. Kawiory 26a, PL-30055 Krakow, Poland
[18]Faculty of Physics and Nuclear Techniques, University of Mining and Metallurgy, PL-30055 Krakow, Poland
[19]Université de Paris-Sud, Lab. de l'Accélérateur Linéaire, IN2P3-CNRS, Bât. 200, FR-91405 Orsay Cedex, France
[20]School of Physics and Chemistry, University of Landcaster, Lancaster LA1 4YB, UK
[21]LIP, IST, FCUL - Av. Elias Garcia, 14-1^o, PT-1000 Lisboa Codex, Portugal
[22]Department of Physics, University of Liverpool, P.O. Box 147, Liverpool L69 3BX, UK
[23]LPNHE, IN2P3-CNRS, Univ. Paris VI et VII, Tour 33 (RdC), 4 place Jussieu, FR-75252 Paris Cedex 05, France
[24]Department of Physics, University of Lund, Sölvegatan 14, SE-223 63 Lund, Sweden
[25]Université Claude Bernard de Lyon, IPNL, IN2P3-CNRS, FR-69622 Villeurbanne Cedex, France
[26]Dipartimento di Fisica, Università di Milano and INFN-MILANO, Via Celoria 16, IT-20133 Milan, Italy
[27]Dipartimento di Fisica, Univ. di Milano-Bicocca and INFN-MILANO, Piazza della Scienza 2, IT-20126 Milan, Italy
[28]IPNP of MFF, Charles Univ., Areal MFF, V Holesovickach 2, CZ-180 00, Praha 8, Czech Republic
[29]NIKHEF, Postbus 41882, NL-1009 DB Amsterdam, The Netherlands
[30]National Technical University, Physics Department, Zografou Campus, GR-15773 Athens, Greece
[31]Physics Department, University of Oslo, Blindern, NO-0316 Oslo, Norway
[32]Dpto. Fisica, Univ. Oviedo, Avda. Calvo Sotelo s/n, ES-33007 Oviedo, Spain
[33]Department of Physics, University of Oxford, Keble Road, Oxford OX1 3RH, UK
[34]Dipartimento di Fisica, Università di Padova and INFN, Via Marzolo 8, IT-35131 Padua, Italy
[35]Rutherford Appleton Laboratory, Chilton, Didcot OX11 OQX, UK
[36]Dipartimento di Fisica, Università di Roma II and INFN, Tor Vergata, IT-00173 Rome, Italy
[37]Dipartimento di Fisica, Università di Roma III and INFN, Via della Vasca Navale 84, IT-00146 Rome, Italy
[38]DAPNIA/Service de Physique des Particules, CEA-Saclay, FR-91191 Gif-sur-Yvette Cedex, France
[39]Instituto de Fisica de Cantabria (CSIC-UC), Avda. los Castros s/n, ES-39006 Santander, Spain
[40]Inst. for High Energy Physics, Serpukov P.O. Box 35, Protvino, (Moscow Region), Russian Federation
[41]J. Stefan Institute, Jamova 39, SI-1000 Ljubljana, Slovenia and Laboratory for Astroparticle Physics,
Nova Gorica Polytechnic, Kostanjeviska 16a, SI-5000 Nova Gorica, Slovenia,
and Department of Physics, University of Ljubljana, SI-1000 Ljubljana, Slovenia
[42]Fysikum, Stockholm University, Box 6730, SE-113 85 Stockholm, Sweden
[43]Dipartimento di Fisica Sperimentale, Università di Torino and INFN, Via P. Giuria 1, IT-10125 Turin, Italy
[44]Dipartimento di Fisica, Università di Trieste and INFN, Via A. Valerio 2, IT-34127 Trieste, Italy
and Istituto di Fisica, Università di Udine, IT-33100 Udine, Italy
[45]Univ. Federal do Rio de Janeiro, C.P. 68528 Cidade Univ., Ilha do Fundão BR-21945-970 Rio de Janeiro, Brazil
[46]Department of Radiation Sciences, University of Uppsala, P.O. Box 535, SE-751 21 Uppsala, Sweden
[47]IFIC, Valencia-CSIC, and D.F.A.M.N., U. de Valencia, Avda. Dr. Moliner 50, ES-46100 Burjassot (Valencia), Spain
[48]Institut für Hochenergiephysik, Österr. Akad. d. Wissensch., Nikolsdorfergasse 18, AT-1050 Vienna, Austria
[49]Inst. Nuclear Studies and University of Warsaw, Ul. Hoza 69, PL-00681 Warsaw, Poland
[50]Fachbereich Physik, University of Wuppertal, Postfach 100 127, DE-42097 Wuppertal, Germany

1 Introduction

In the framework of the Standard Model (SM) there is one physical Higgs boson, H, which is a neutral CP-even scalar. At LEP2 the main production process is through the s-channel, $e^+e^- \rightarrow Z^* \rightarrow HZ$, but there are additional t-channel diagrams in the $H\nu\bar{\nu}$ and He^+e^- final states, which proceed through W^+W^- and ZZ fusion, respectively. With the data taken previously up to $\sqrt{s} = 188.7$ GeV, DELPHI excluded a SM Higgs boson with mass less than 94.6 GeV/c^2 [1] at the 95% confidence level (CL). The other LEP collaborations reached similar results [2]. The present analysis concentrates on masses between 85 and 115 GeV/c^2. The results obtained in the same mass range with the data taken by DELPHI in the last year of LEP operation and analysed with preliminary calibration constants can be found in [3]. Although the emphasis is on high masses, the analysis described in this paper is also applied to lower masses, down to the $b\bar{b}$ threshold, in order to derive a constraint on the production cross-section of a SM-like Higgs boson as a function of its mass.

In the Minimal Supersymmetric Standard Model (MSSM), the production of the lightest scalar Higgs boson, h, proceeds through the same processes as in the SM. The results of the search for the SM Higgs boson thus also apply to the h boson. However, in the MSSM the production cross-section is reduced with respect to the SM one and even vanishes in part of the MSSM parameter space. This model predicts also a CP-odd pseudo-scalar, A, that would be produced mostly in the $e^+e^- \rightarrow Z^* \rightarrow hA$ process at LEP2. The MSSM parameters are such that when the single h production is suppressed, the associated hA production is enhanced. This channel is thus also considered in this paper. Previous 95% CL limits from DELPHI on the masses of h and A of the MSSM were 82.6 GeV/c^2 and 84.1 GeV/c^2 respectively [1]. The results of the other LEP collaborations are described in Ref. [2]. The present analysis in the hA channel concentrates on masses between 80 and 95 GeV/c^2.

In the HZ channel, all known decays of the Z boson have been taken into account (hadrons, charged leptons and neutrinos) while the analyses have been optimised either for decays of the Higgs particle into $b\bar{b}$, making use of the expected high branching fraction of this mode, or for Higgs boson decays into a pair of τ's, which is the second main decay channel in the SM and in most of the MSSM parameter space. A dedicated search for the Higgs boson invisible decay modes will be reported separately. The hA production has been searched for in the two main decay channels, namely the 4b and $b\bar{b}\tau^+\tau^-$ final states.

2 Data samples and detector overview

In 1999 LEP ran at centre-of-mass energies ranging from 191.6 GeV to 201.7 GeV. DELPHI recorded 25.9 pb^{-1} at 191.6 GeV, 76.9 pb^{-1} at 195.6 GeV, 84.3 pb^{-1} at 199.6 GeV and 41.1 pb^{-1} at 201.7 GeV. The requirement of full detector performance reduces the luminosities in the He^+e^- and $H\nu\bar{\nu}$ searches by at most 3%. The detector was unchanged from the previous data taking period. Ref. [4] provides a short description while more details can be found in Ref. [5,6] for the original setup and in Ref. [7] for the LEP2 upgrade of the silicon tracking detector.

Large numbers of background and signal events have been produced by Monte Carlo simulation and then passed through the DELPHI detector simulation program [5]. These samples typically correspond to about 100 times the luminosity of the collected data. Backgrounds were generated with `PYTHIA` [8] for hadronic two-fermion final states and

with KORALZ [9] for leptonic two-fermion final states. The four-fermion background was generated with EXCALIBUR [10] in most of the phase space, but GRC4F [11] and KORALW [12] were used to complete the EXCALIBUR samples in the case of very forward electrons or low mass hadronic resonances, respectively. TWOGAM [13] and BDK [14] were used for two-photon processes and BHWIDE [15] for Bhabha events in the main acceptance region.

Signal events were produced using the HZHA [16] generator. As the enhancement in the production cross-section due to W^+W^- fusion is significant in the $H\nu\bar{\nu}$ channel [17] (e.g. 20% for m_H at the HZ kinematic threshold), signal events in this channel were generated using a version of HZHA modified to include also fusion and interference between the HZ and W^+W^- fusion diagrams. For the HZ process, the H mass was varied from 12 to 115 GeV/c^2, while for hA the range for the A mass was 12 to 95 GeV/c^2. A step of 5 GeV/c^2 was used above 80 GeV/c^2, since the analyses were optimized at high mass. Wider steps were used at lower masses. Moreover, the hA signal events were simulated for three values of $\tan\beta$ (the ratio of the vacuum expectation values of the two Higgs field doublets of the MSSM) equal to 2, 20 or 50. This fixes the h mass, almost equal to m_A for $\tan\beta = 20$, 50 and lower than m_A by around 20 GeV/c^2 if $\tan\beta = 2$. The h and A widths are lower than 1 GeV/c^2 for $\tan\beta$ below 20 and increase rapidly to reach several GeV/c^2 at $\tan\beta = 50$, thus going above the experimental mass resolution which is typically of 3 GeV/c^2 in the hA channels.

The HZ simulated samples were classified according to the Higgs and Z boson decay modes. For He^+e^-, $H\mu^+\mu^-$ and $H\nu\bar{\nu}$ the natural SM mix of H decay modes into fermions was permitted. As final states with hadrons and two τ's benefit from a dedicated analysis, the $\tau\tau$ decay mode was removed in the $Hq\bar{q}$ channel simulations and we generated separately the two HZ channels involving τ leptons for which one of the bosons is forced to decay to τ's and the other hadronically. Finally, the hA simulations cover final states involving either four b quarks or two b quarks and two τ's, irrespective of which Higgs boson decays into τ's. Efficiencies are defined relative to these states. The sizes of these samples vary from 2000 to 3000 events and they were produced at the four centre-of-mass energies.

Although the above signal simulations cover most of the expected final states in the SM and MSSM, they were completed by two additional sets at 199.6 GeV. We generated hA samples with large mass differences between the h and A bosons, as expected when scanning the MSSM parameter space more widely than in the representative scans, and hZ samples with $h \to AA$, as expected in restricted regions of the MSSM parameter space. In these two sets, the A (h) mass was varied from 12 GeV/c^2 (50 GeV/c^2) up to the kinematic limit and only the main decays were simulated; the hA samples were restricted to four b final states, and the $(h \to AA)Z$ samples to hadronic decays of the Z boson and either four b or four c quarks from the A pair. The results obtained from these samples were assumed to be valid also at the three other centre-of-mass energies.

3 Features common to all analyses

3.1 Particle selection

In all analyses, charged particles are selected if their momentum is greater than 100 MeV/c and if they originate from the interaction region (within 4 cm in the transverse plane and within 4 cm / $\sin\theta$ along the beam direction, where θ is the particle polar angle). Neutral particles are defined either as energy clusters in the calorimeters not associated to charged particle tracks, or as reconstructed vertices of photon conversions,

interactions of neutral hadrons or decays of neutral particles in the tracking volume. All neutral clusters of energy greater than 200 or 300 MeV (depending on the calorimeter) are used. The $\pi^{\pm}$ mass is used for all charged particles except identified leptons, while zero mass is used for electromagnetic clusters and the K^0 mass is assigned to neutral hadronic clusters.

3.2 b-quark identification

The method of separation of b quarks from other flavours is described in [18], where the various differences between B-hadrons and other particles are accumulated in a single variable, hereafter denoted x_{b} for an event and x_{b}^i for jet i. A major input to this combined variable is the probability P_i^+ that all tracks with a positive lifetime-signed impact parameter in the jet lead to a product of track significances as large as that observed, if these tracks do originate from the interaction point. A low value of this probability is a signature for a B-hadron. The likelihood ratio technique is then used to construct x_{b}^i by combining P_i^+ with information from any secondary vertex found in the jet (the mass computed from the particles assigned to the secondary vertex, the rapidity of those particles, and the fraction of the jet momentum carried by them) and with the transverse momentum (with respect to the jet axis) of any lepton belonging to the jet. The event variable, x_{b}, is a linear combination of the jet variables. Increasing values of x_{b} (or x_{b}^i) correspond to increasingly 'b-like' events (or jets).

The procedure is calibrated on events recorded in the same experimental conditions at the Z resonance. The performance of the combined b-tagging is described in Ref. [19] and that of the impact parameter tagging alone in Ref. [20]. The overall performance of the combined b-tagging for 1999 Z data is illustrated in Fig. 1. Data agree with simulation to better than 5% in the whole range of cut values.

3.3 Constrained fits

In most channels a constrained fit [21] is performed to reconstruct the Higgs boson mass, and often to reject background processes as well. In order to allow the removal of most of the events involving radiative return to the Z, an algorithm has been developed [22] in order to estimate the effective energy of the e^+e^- collision. This algorithm makes use of a three-constraint kinematic fit in order to test the presence of an initial state photon along one of the beam directions and hence lost in the beam pipe. This effective centre-of-mass energy is called $\sqrt{s'}$ throughout this paper.

3.4 Confidence level definitions and calculations

The confidence level definitions rely on a test-statistic built with the likelihood ratio technique [23]. Let $\mathcal{Q}$ be the ratio of the likelihood of the observed candidates assuming signal plus background to that found using the background-only hypothesis. $\mathcal{Q}$ classifies the result of an observation between the background-like and signal plus background-like situations. We then define the confidence level for the background hypothesis, $\mathrm{CL_b}$, as the probability, in background-only experiments, to obtain equal or smaller values of $\mathcal{Q}$ (that is more background-like results) than that observed. Similarly, the confidence level for the signal plus background hypothesis, $\mathrm{CL_{s+b}}$, is the probability, in signal plus background experiments, to obtain more background-like results than those observed. The pseudo-confidence level for the signal hypothesis, $\mathrm{CL_s}$, is conservatively defined as

the ratio of these two probabilities, CL_{s+b}/CL_b. CL_s measures the confidence with which the signal hypothesis can be rejected and must fall below 5% for an exclusion confidence of 95%. More technical details about how the confidence levels are calculated or how uncertainties are taken into account can be found in [4].

In the definition of the test-statistic $\mathcal{Q}$, two-dimensional discriminant information is used in all channels, as in our previous publication [1]. The first variable is the reconstructed Higgs boson mass (or the sum of the reconstructed h and A masses in the hA channels), the second one is channel-dependent, as specified in the following sections. In order to make full use of the information contained in the second variable, the final selections are loose: the method used for deriving the confidence levels ensures that adding regions of lower signal and higher background can only enhance the performance relative to a tighter selection.

The distributions are represented as two-dimensional histograms which are derived from the simulation samples. These distributions are then smoothed using a two-dimensional kernel, which is essentially Gaussian but with a small component of a longer tail. The width of the kernel varies from point to point, such that the statistical error on the estimated background is never more than 30%. Finally the distribution is reweighted so that when projected onto either axis it has the same distribution as would have been observed if the smoothing had been only in one dimension. This makes better use of the simulation statistics if there are features which are essentially one dimensional, such as mass peaks. A check for residual statistical fluctuations was made by dividing the simulation into sub-samples, and comparing the expected results; no significant effects were observed.

4 Higgs boson searches in events with jets and electrons

The analysis is based upon the same electron identification algorithm and discriminant variables as in [4,1] and is briefly described in the following. The preselection requires at least 8 charged particles, a total energy above $0.12\sqrt{s}$ and at least a pair of loose electron candidates of energies above 10 GeV and impact parameters below 2 mm (1 cm) in the transverse plane (along the beam direction). The Bhabha veto and the modified selections allowing for the tau decays of the Higgs boson are as described in [1]. To reduce the $Z\gamma^*$ and $q\bar{q}(\gamma)$ backgrounds, the sum of the di-electron and hadronic system masses must be above 50 GeV/c^2, while the missing momentum is required to be below 50 GeV/c if its direction is within 10° to the beam axis. The jet reconstruction and selection proceed as in [4].

After this preselection, each pair of electron candidates with opposite charges is submitted to further cuts. The electron identification is first tightened, allowing at most one electron candidate in the insensitive regions of the calorimeter. The two electrons are required to have energies above 20 GeV and 15 GeV, respectively. Electron isolation angles with respect to the closest jet are required to be more than 20° for the more isolated electron and more than 8° for the other one. A five-constraint kinematic fit is performed to test the compatibility of the e^+e^- invariant mass with the Z mass; the fit imposes energy and momentum conservation and takes into account the Breit-Wigner shape of the Z resonance [1]. Events with a fit probability below 10^{-8} are rejected. As the search is restricted to high mass Higgs bosons produced in association with a Z particle, the sum of the fitted masses of the electron pair and of the hadronic system is required to

be above 150 GeV/c^2 and their difference in the range from -100 GeV/c^2 to 50 GeV/c^2. The fitted hadronic mass and the b-tagging variable x_b are used in the two-dimensional calculation of the confidence levels.

The effect of the selections on data and simulated samples are detailed in Tables 1 to 4, while the efficiencies at the end of the analysis are reported in Tables 5 and 6 as a function of m_{H}. The agreement between data and simulation at the preselection level is illustrated in Fig. 2 which shows the distributions of the electron energies, the fitted mass of the jet system and the isolation angle of the more isolated electron candidate. At the end of the analysis, 11 events are selected in the data for a total expected background of $11.5 \pm 0.2(stat.)$ events coming mainly from the $\mathrm{e^+e^-q\bar{q}}$ process.

The systematic uncertainties on background and efficiency estimates are mainly due to the imperfect simulation of the detector response and were estimated as described in [4]. The relative error on the efficiencies is $\pm 3\%$ while that on the background estimates at each centre-of-mass energy is $\pm 7\%$.

5 Higgs boson searches in events with jets and muons

The analysis follows that published in [4,1], with slight modifications in the preselection to adapt to somewhat different beam conditions in 1999. The preselection requires at least 9 charged particles with two of them in the central part of the detector ($40\,^\circ < \theta < 140\,^\circ$) and at least two high quality tracks of particles with a transverse momentum greater than 5 GeV/c. For high quality tracks, impact parameters less than 100 μm in the transverse plane and less than 500 μm along the beam direction are required. The rest of the preselection is unchanged and requires at least two particles of opposite charges and momenta greater than 15 GeV/c.

The rest of the analysis is based upon the same muon identification algorithm and discriminant variables as in [4], but the selection criteria have been re-optimised [4]. As a result, the level of muon identification corresponds now to an efficiency of 88% and a misidentification probability of 8.8% per pair of muon candidates. At least two muons are required with opposite charges, an opening angle larger than 10°, and momenta greater than 34 GeV/c and 21 GeV/c. The jet reconstruction and selection proceed as in [4]. Finally, the angle with respect to the closest jet axis must be greater than 9° for the more isolated muon and greater than 7° for the other one. A five-constraint kinematic fit taking into account energy and momentum conservation and the Breit-Wigner shape of the Z resonance is then performed to test the compatibility of the di-muon mass with the Z mass in a window of ± 30 GeV around the Z pole. Events are kept only if the fit converges in this mass window. As in the electron channel, the fitted mass of the hadronic system and the b-tagging variable x_{b} are chosen as the discriminant variables for the two-dimensional calculation of the confidence levels.

The effect of the selections on data and simulated samples are detailed in Tables 1 to 4, while the efficiencies at the end of the analysis are reported in Tables 5 and 6 as a function of m_{H}. The agreement of simulation with data is quite good, as illustrated at preselection level in Fig. 3, which shows the multiplicity of the charged particles, the momentum of the higher-momentum particle in any preselected pair, the isolation angle of the more isolated particle in any preselected pair and the b-tagging variable x_{b}. At the end of the analysis, 8 events are selected in data in agreement with the total expected background of $9.4 \pm 0.1(stat.)$ events coming mainly from the $\mu^+\mu^-\mathrm{q\bar{q}}$ process.

The imperfect simulation of the detector response leads to systematic errors in background and efficiency evaluation. As explained in [4], each of the momentum and angular

cuts was varied in a range given by the difference between the mean values of the simulated and real data distributions of the corresponding variable at preselection level. The muon pair identification level, which is a discrete variable, was modified randomly with a probability of 5%, corresponding to the maximum difference observed in muon identification results when comparing data with simulation. This appears to be the main source of systematic uncertainty. For the efficiencies, a relative error of $\pm 2\%$ can be quoted, independent of m_{H}, while the relative error on the expected backgrounds at each centre-of-mass energy is $\pm 3\%$.

6 Higgs boson searches in events with jets and taus

Three channels are covered by these searches, two for the HZ channel, depending on which boson decays into $\tau^+\tau^-$, and one for the hA channel. The analysis, identical to that described in [1], selects hadronic events by requiring at least ten charged particles, a total reconstructed energy greater than $0.4\sqrt{s}$, a reconstructed charged energy above $0.2\sqrt{s}$ and $\sqrt{s'}$ greater than 120 GeV.

A search for τ lepton candidates is then performed using a likelihood ratio technique. Single charged particles are preselected if they are isolated from all other charged particles by more than 10°, if their momentum is above 2 GeV/c and if all neutral particles in a 10° cone around their direction make an invariant mass below 2 GeV/c^2. The likelihood variable is calculated for the preselected particles using distributions of the particle momentum, of its isolation angle and of the probability that it comes from the primary vertex. As an illustration of the agreement between data and simulation at this level of the analysis, Fig. 4a shows the distribution of the isolation angle of the preselected charged particle with the highest τ likelihood variable in the event. Pairs of τ candidates are then selected requiring opposite charges, an opening angle greater than 90° and a product of the τ likelihood variables above 0.45. If more than one pair is selected, only the pair with the highest product is kept. The distribution of the highest product of two τ likelihood variables in the event is given in Fig. 4b. The discrimination between the Higgs signal and the SM background is clearly visible. Moreover, the percentage of τ pairs correctly identified is over 90% in simulated Higgs events.

Two slim jets are then reconstructed with all neutral particles inside a 10° cone around the directions of the τ candidates. The rest of the event is forced into two jets using the DURHAM algorithm. The slim jets are required to be in the $20° \leq \theta_\tau \leq 160°$ polar angle region to reduce the $\mathrm{Ze^+e^-}$ background, while the hadronic di-jet invariant mass is required to be between 20 and 110 GeV/c^2 in order to reduce the $\mathrm{q\bar{q}}(\gamma)$ and $\mathrm{Z}\gamma^*$ backgrounds. The jet energies and masses are then rescaled, imposing energy and momentum conservation, to give a better estimate of the masses of both di-jets ($\tau^+\tau^-$ and $\mathrm{q\bar{q}}$), that are required to have a rescaled mass above 20 GeV/c^2, and below $\sqrt{s}$ to discard unphysical solutions of the rescaling procedure. Each hadronic jet must have a rescaling factor in the range 0.4 to 1.5.

The remaining background comes from genuine $\ell^+\ell^-\mathrm{q\bar{q}}$ events. In order to reject the $\mathrm{e^+e^-q\bar{q}}$ and $\mu^+\mu^-\mathrm{q\bar{q}}$ backgrounds the measured mass of the leptonic system is required to be between 10 and 80 GeV/c^2 and its electromagnetic energy to be below 60 GeV (see Fig. 4c). This terminates the selection procedure. The effect of the selections on data and simulated samples are detailed in Tables 1 to 4, while the efficiencies at the end of the analysis in the three $\tau^+\tau^-\mathrm{q\bar{q}}$ channels are reported in Tables 5, 6 and 8 as a function of the Higgs boson masses. At the end of the analysis, 6 events are selected in data for

a total expected background of $6.9 \pm 0.2(stat.)$ events coming mainly from the $\tau^+\tau^-\mathrm{q}\bar{\mathrm{q}}$ and $\tau\nu\mathrm{q}'\bar{\mathrm{q}}$ processes.

Systematic uncertainties from the imperfect modelling of the detector response were estimated by moving each selection cut according to the resolution in the corresponding variable. The main contributions arise from the cuts on the $\tau^+\tau^-$ invariant mass and electromagnetic energy. The total relative systematic uncertainties amount to $\pm 6\%$ on signal efficiencies and $\pm 11\%$ on the background estimates at each centre-of-mass energy.

The two-dimensional calculation of the confidence levels uses the reconstructed mass given by the sum of the $\tau^+\tau^-$ and $\mathrm{q}\bar{\mathrm{q}}$ di-jet masses after rescaling and a likelihood variable built from the distributions of the rescaling factors of the τ jets, the τ momenta and the global b-tagging variable, x_b. The distribution of this likelihood variable at the end of the analysis is shown in Fig. 4d to illustrate the discrimination between the Higgs signal and the SM backgrounds. Since the three possible $\tau^+\tau^-\mathrm{q}\bar{\mathrm{q}}$ signals are covered by the same analysis, the three channels cannot be considered as independent in the confidence level computation. For this computation, they are combined into one global $\tau^+\tau^-\mathrm{q}\bar{\mathrm{q}}$ channel: at each test point, the signal expectations (rate, two-dimensional distribution) in this channel are obtained by summing the contributions from the three original signals weighted by their expected rates.

7 Higgs boson searches in events with missing energy and jets

Events due to particles of the beam with momenta far from the nominal values are first excluded by requiring at least two charged particles with impact parameters less than 1 mm in the transverse plane and less than 3 mm along the beam direction, and with a transverse momentum greater than 2 GeV/c. A loose hadronic preselection is then applied, requiring at least nine charged particles, a total charged energy greater than $0.16\sqrt{s}$, a transverse energy greater than $0.15\sqrt{s}$ and the sum of the magnitudes of all particle momenta resolved along the thrust axis to be greater than $0.25\sqrt{s}$. Finally, events with an electromagnetic shower exceeding $0.45\sqrt{s}$ are rejected. These criteria remove 97% of the $\gamma\gamma$ background and veto completely the Bhabha background.

In order to reject events coming from a radiative return to the Z with photons emitted in the beam pipe, $\sqrt{s'}$ is required to be greater than 115 GeV when the polar angle of the missing momentum is within 40° to the beam axis. To reduce the contamination of radiative return events with photons in the detector acceptance, events are rejected if their total electromagnetic energy within 30° to the beam axis is greater than $0.16\sqrt{s}$ or if the total energy in the small angle luminosity monitor is greater than $0.08\sqrt{s}$. A veto based on the hermeticity counters of DELPHI as described in [20] is also applied to reject events with photons crossing the small insensitive regions of the electromagnetic calorimeters. To reduce the two-fermion background outside the radiative return peak as well as four-fermion backgrounds without missing energy, $\sqrt{s'}$ must not exceed $0.96\sqrt{s}$. Two-fermion events with jets pointing to the insensitive regions of the electromagnetic calorimeters are also a potential background due to mismeasurements of the jet properties. To reject such a background, events are forced into a two-jet configuration using the DURHAM algorithm and are rejected if the jet polar angles are within ±5° of 40° for one jet and of 140° for the other jet, unless the acoplanarity [1] is greater than 10°. At this stage, 88%

[1] The acoplanarity is defined as the supplement of the angle between the transverse momenta (with respect to the beam axis) of the two jets.

of the total $q\bar{q}(\gamma)$ background is removed. In order to reduce most of the contamination from semi-leptonic decays of W^+W^- pairs, the energy of the most energetic particle of the event must not exceed $0.2\sqrt{s}$. To reinforce the rejection of those decays containing a τ lepton, there must be no charged particle in the event with a transverse momentum with respect to its jet axis greater than 10 GeV/c when forcing the event into the two-jet configuration. The final selection of signal-like events requires the total visible energy to be lower than $0.70\sqrt{s}$. All the above criteria define the preselection.

The final discrimination between signal and background is achieved through a multi-dimensional variable built with the likelihood ratio method. A short description of the algorithms needed in this step is given below. As already mentioned, events are forced into two jets with the DURHAM algorithm (the so called "two-jet configuration") but for each event jets are also reconstructed with the same algorithm using a distance of $y_{cut} = 0.005$ (the so called "free-jet configuration") and general variables of each jet (like multiplicities, momenta) are calculated in both configurations. In order to tag remaining isolated particles from semi-leptonic decays of W^+W^- pairs, the energies collected between two cones with half opening angles of 5° and 25° around the most isolated and the most energetic particles are calculated and normalised to the corresponding particle energies. The lesser of these two normalised energies defines the anti-W^+W^- isolation variable.

The likelihood multidimensional variable combines the following discriminant variables: the angle between the missing momentum and the closest jet in the free-jet configuration, the polar angle of the more forward jet in the two-jet configuration, the polar angle of the missing momentum, the acoplanarity in the two-jet configuration, the ratio between $\sqrt{s'}$ and the centre-of-mass energy, the missing mass of the event, the anti-W^+W^- isolation variable, the largest transverse momentum with respect to its jet axis of any charged particle in the two-jet configuration, the DURHAM distance for the transition betwen the two-jet and three-jet configurations, the minimum jet charged multiplicity in the free-jet configuration, the event lifetime probability P_E^+ that all tracks with a positive lifetime-signed impact parameter in the event give a product of track significances as large as that observed if they do come from the interaction point, and the global b-tagging variable x_{b}. The first five variables discriminate the signal from the $q\bar{q}(\gamma)$ background and the other variables provide a discrimination against W^+W^- pairs. For each variable, probability density functions (p.d.f.s) at each centre-of-mass energy are obtained from simulated events, using half of the statistics available in all backgrounds and in signals of masses 95, 100 and 105 GeV/c^2 at $\sqrt{s}$ below 198 GeV, and 100, 105, 110 and 115 GeV/c^2 for $\sqrt{s}$ above 198 GeV. The whole samples are used to derive the final results, in order to improve limited statistics in some bins of the two-dimensional discriminant information used to derive the confidence levels.

The distributions of four of the input variables are shown at preselection level in Fig. 5, while Fig. 6 shows the distribution of the likelihood discriminant variable. The comparison between the observed and expected rates in the signal-like tail of this distribution is illustrated further in Fig. 6, which shows the observed and expected background rates at $\sqrt{s} = 199.6$ GeV/c^2 as a function of the efficiency for a Higgs signal of 105 GeV/c^2 when varying the cut on the likelihood variable. As a final selection, a minimal value of 1.0 is required, leaving 108 events in data for a total expected background of $105.7 \pm 1.2(stat.)$. The two-dimensional calculation of the confidence levels uses the likelihood variable and the recontructed Higgs boson mass defined as the visible mass given by a one-constraint fit where the recoil system is an on-shell Z boson. The effect of the selections on data

and simulated samples are detailed in Tables 1 to 4, while the efficiencies at the end of the analysis are reported in Tables 5 and 6 as a function of m_{H} .

Systematic uncertainties due to the use of non-independent samples in the definition of the p.d.f.s and in the final result derivation were estimated by comparing the results when running the analysis on the reference samples and on the complementary samples. The differences between the two sets of results are then quoted as systematics if they are higher than the statistical uncertainties. These systematics amount to $\pm 2.0\%$ for the efficiencies and to $\pm 4.5\%$ for the background estimates at $\sqrt{s} = 191.6$ and 201.7 GeV/c^2 while no significant difference is observed for the background estimates at the other two energies. Systematic uncertainties due to the imperfect modelling of the detector response were derived by rescaling the bin contents of each p.d.f. from simulation to those in data, restricting to bins where the deviation between data and simulation exceeded two standard deviations. The analysis was then repeated with the rescaled p.d.f. for each variable in turn and the largest difference with respect to the initial result taken as systematics. These amount to $\pm 2.0\%$ on the efficiencies and $\pm 10.0\%$ on the background estimates and come from the p.d.f. of the acoplanarity. It was checked that these differences remained similar with tighter selections in the likelihood variable. Thus the overall uncertainties are $\pm 3.0\%$ on the efficiencies, $\pm 10.0\%$ ($\pm 11.0\%$) on the background estimates at $\sqrt{s} = 195.6$ and 199.6 GeV/c^2 (191.6 and 201.7 GeV/c^2).

A second analysis using the same preselection criteria followed by an Iterated nonlinear Discriminant Analysis (IDA) as described in [4] gave similar results.

8 Higgs boson searches in pure hadronic events

Higgs boson searches in pure hadronic final states start with a common four-jet preselection, which eliminates $\gamma\gamma$ events and reduces the $\mathrm{q\bar{q}}(\gamma)$ and $\mathrm{Z}\gamma^*$ backgrounds. As this step did not change since the previous analysis, the reader is referred to [4,1] for the exact description of the cuts and only the important features are briefly mentioned here. After a selection of multi-hadron events excluding those with an energetic photon in the calorimeters or lost in the beam pipe, topological criteria are applied to select multi-jet events. All selected events are then forced into a four-jet topology with the DURHAM algorithm and a minimal multiplicity and mass is required for each jet. After the preselection, different analysis procedures are applied in the HZ and hA channels.

8.1 The HZ four-jet channel

After the common four-jet preselection, events are selected using a discriminant variable defined as the output of an artificial neural network [24] which combines four variables. Three of them are introduced to reduce the four-fermion contamination. The first relies on b-tagging and is the maximum b-tagging variable of any di-jet in the event, a di-jet b-tagging variable being defined as the sum of the two jet b-tagging variables, x_{b}^i. The second and third variables rely on mass information and test the compatibility of the event with the hypotheses of $\mathrm{W^+W^-}$ and ZZ pair-production, respectively. First, constrained fits are used to derive the probability density function measuring the compatibility of the event kinematics with the production of two objects of any masses. This two-dimensional probability, called the ideogram probability, is then folded with the expected mass distributions for the $\mathrm{W^+W^-}$ and ZZ processes, respectively. More about the ideogram technique can be found in [25]. Finally, the fourth input variable to the neural

network is intended to reduce the $q\bar{q}(\gamma)$ contamination and is the output of another neural network [26] (anti-QCD neural network) constructed from eight variables. These are mostly shape or jet variables: the sum of the second and fourth Fox-Wolfram moments, the product of the minimum jet energy and the minimum opening angle between any two jets, the maximum and minimum jet momenta, the sum of the multiplicities of the two jets with lowest multiplicity and the sum of the masses of the two jets with lowest masses. For the last two variables, the six possible pairings of the jets are considered and the variables are defined as the minimum di-jet mass and the minimum sum of the cosines of the opening angles of the two dijets in any pairing. As the discrimination between the $q\bar{q}(\gamma)$ background and the $Hq\bar{q}$ signal provided by these variables depends mainly on the difference $\sqrt{s}-m_{\rm H}$, the anti-QCD neural network was trained with simulations at $\sqrt{s}$ = 189 GeV, using $q\bar{q}(\gamma)$ events and 95 GeV/c^2 $Hq\bar{q}$ events. In order to minimize the risk of overtraining, the neural network used for the final discrimination was trained with fractions of the available simulated samples at $\sqrt{s} = 195.6$ GeV in $q\bar{q}(\gamma)$ background (10%), four-fermion background (50%), and 105 GeV/c^2 $Hq\bar{q}$ signal (50%). The whole samples were used to derive the final results.

The agreement between data and background simulation after the four-jet preselection is illustrated in Fig. 7 which shows the distributions of three analysis variables and of the recontructed Higgs boson mass obtained as explained below. Fig. 8 shows the distribution of the final neural network output variable and, as an example, the expected background rate and the data at $\sqrt{s} = 199.6$ GeV, as a function of the efficiency for a 105 GeV/c^2 signal when varying the cut on the neural network output variable. As a final selection, a minimal value of 0.3 is required. This suppresses the most background-like events, leaving 161 events in data and a total expected background of $175.4 \pm 1.3(stat.)$. The effect of the selections on data and simulated samples are detailed in Tables 1 to 4, while the efficiencies at the end of the analysis are reported in Tables 5 and 6 as a function of $m_{\rm H}$ for the $Hq\bar{q}$ channel and in Table 7 as a function of $m_{\rm H}$ and $m_{\rm A}$ for the $(h \rightarrow AA)$ $q\bar{q}$ channels. Since these two channels, specific to the MSSM, are covered by the same analysis as that of the $Hq\bar{q}$ channel, the three channels cannot be considered as independent in the confidence level computation when testing MSSM models. For this computation, they are combined into one global $Hq\bar{q}$ channel: at each test point, the signal expectations (rate and two-dimensional distribution as defined below) in this channel are obtained by summing the contributions from the three original signals weighted by their expected rates.

The two-dimensional calculation of the confidence levels uses the final neural network variable and the recontructed H boson mass estimated as follows. For each of the six possible pairings of jets into an HZ pair, a kinematic fit is applied, requiring energy and momentum conservation and one di-jet to be at the nominal Z mass. The pairing of jets defining the Higgs boson and Z candidates is then that which maximises the probability [4] that both the b-content of the different jets and the χ^2 probability of the five-constraint fit are compatible with the production of an HZ pair.

The systematic uncertainties from the imperfect modelling of the detector response were estimated by repeating the selection procedure on the distribution of the neural network variable obtained by smearing, in turn, each of the distributions of the three input variables according to the resolution in the variable. This leads to relative uncertainties of $\pm 6.0\%$ related to b-tagging, $\pm 3.0\%$ related to the anti-QCD variable and $\pm 2.5\%$ related to the WW ideogram probability. This results in an overall relative uncertainty of $\pm 7.2\%$ in the background and efficiency estimates at each centre-of-mass energy.

8.2 The hA four-b channel

The analysis is very similar to that published in [1]. After the common four-jet preselection, events are preselected further, requiring a visible energy greater than 120 GeV, $\sqrt{s'}$ greater than 150 GeV, a missing momentum component along the beam direction lower than 30 GeV/c and at least two charged particles per jet. A four-constraint kinematic fit requiring energy and momentum conservation is then applied, and the two di-jet masses are calculated for each of the three different jet pairings. As the possible production of MSSM Higgs bosons through the hA mode dominates at large $\tan\beta$ where the two bosons are almost degenerate in mass, the pairing defining the Higgs boson candidates is chosen as that which minimizes the mass difference between the two di-jets. The final discrimination between background and signal is then based on a multidimensional variable which combines the following eight variables with a likelihood ratio method: the event thrust, the second and fourth Fox-Wolfram moments, the difference between the Higgs boson candidate masses as given by the kinematic fit, the production angle of the Higgs boson candidates, the sum of the four jet b-tagging variables, the minimum di-jet b-tagging variable and the number of secondary vertices. For each variable, probability density functions (p.d.f.s) were obtained from simulated events, using fractions of the statistics available in the $q\bar{q}(\gamma)$ background (40%) and four-fermion background (80%) at $\sqrt{s}$ = 195.6 GeV and 199.6 GeV and in signal events with m_A = 85, 90 GeV/c^2 and $\tan\beta$ =20 (50%) at $\sqrt{s}$ = 195.6 GeV. The whole samples were used to derive the final results.

The agreement between data and background simulation after the preselection is illustrated in Fig. 9 which shows the distributions of three input variables and of the sum of the recontructed Higgs boson masses as given by the kinematic fit. Fig. 10 shows the distribution of the final discriminant variable and, as an example, the expected background rate and the data at $\sqrt{s}$ = 199.6 GeV, as a function of the efficiency for a signal with m_A= 85 GeV/c^2 and $\tan\beta$ = 20, when varying the cut on the discriminant variable. As a final selection, a minimal value of 0.1 is required, leading to 136 events in data, for a total expected background of $137.8 \pm 1.2(stat.)$. The effect of the selections on data and simulated samples are detailed in Tables 1 to 4, while the efficiencies at the end of the analysis are reported in Tables 8 and 9 as functions of m_A and $\tan\beta$ and of m_A and m_h.

The two-dimensional calculation of the confidence levels uses the likelihood variable and the sum of the reconstructed Higgs boson masses as given by the kinematic fit.

Systematic uncertainties due to the use of non-independent samples in the definition of the p.d.f.s and in the final result derivation were estimated at the level of ±4.0% relative, by repeating the whole procedure with two independent samples of lower size. Systematic uncertainties due to the imperfect modelling of the detector response were derived as in the previous section. The uncertainty related to b-tagging amounts to ±5.0% and that related to shape variables to ±3.0%, resulting in an overall relative uncertainty of ±7.0% on background and efficiency estimates at each centre-of-mass energy.

9 Results

The results of the searches presented in the previous sections can be translated into exclusion limits on the masses of the neutral Higgs bosons in the SM and MSSM.

9.1 Reconstructed mass spectra

As an illustration of the discrimination achieved against the residual SM background, distributions of the reconstructed Higgs boson mass(es) after tight selections are presented in Fig. 11 in the HZ and hA channels. The selections correspond to requiring a minimal b-tagging value of -1.8 in the He^+e^- and $H\mu^+\mu^-$ channels, minimal likelihood values of 0.8, 7.0 and 3.5 in the $\tau^+\tau^-q\bar{q}$, $H\nu\bar{\nu}$ and 4b channels, respectively, and a minimal neural network output of 0.85 in the $Hq\bar{q}$ channel. The corresponding observed and expected rates at each of the four centre-of-mass energies are summarized in Table 10.

9.2 The SM Higgs boson

We proceed to set a limit on the SM Higgs boson mass, combining the data analysed in the previous sections with those taken at lower energies, namely 161.0, 172.0 GeV [20], 182.7 GeV [4] and 188.7 GeV [1]. The expected cross-sections and branching ratios are taken from the database provided by the LEP Higgs working group, using the `HZHA` [16] package, Version 3, with the top mass set to 174.3 GeV/c^2.

Curves of the confidence level CL_b and CL_s as a function of the test mass m_{H} are shown in Fig. 12. In the presence of a sizeable Higgs signal, the value of the observed CL_b (top of Fig. 12) would approach one, since it measures the fraction of background-only experiments which are more background-like than the observation. Here the compatibility between the observation and the expectation from background-only is well within one standard deviation over the range of masses tested. Moreover, the mass giving an expected 5σ discovery, defined by the intersection of the curve for signal plus background experiments with the horizontal line at $1 - CL_b = 5.7 \times 10^{-7}$, is 98.2 GeV/$c^2$. The pseudo-confidence level in the signal is shown in Fig. 12 (bottom). The observed 95% CL lower limit on the mass is 107.3 GeV/c^2 while the expected median limit is 106.4 GeV/c^2.

The curve of the test-statistic $\mathcal{Q}$ as a function of the mass hypothesis is shown in Fig. 13, where the observation is compared with the expectations from background-only experiments (top) and from signal plus background experiments (bottom). Over the whole range of masses, the test-statistic remains positive, while in the event of a discovery it would be negative for mass hypotheses close to the actual mass of the signal.

9.3 Cross-section limit

In a more general approach, the results of the searches for a SM Higgs boson can be used to set a 95% CL upper bound on the Higgs boson production cross-section, assuming that the Higgs boson decay properties are identical to those in the SM but that the Higgs boson couplings to pairs of Z and $W^{\pm}$ bosons (the latter arising in the W^+W^- fusion production mechanism) may be smaller. To achieve the best sensitivity over the widest range of mass hypotheses, the results described in this paper are combined with those obtained at lower energies at LEP2 [1,4,20], as well as with those obtained at LEP1 [27] which covered masses up to 60 GeV/c^2. Both sets of results are treated with the same statistical procedure as for the SM. For each mass hypothesis, the production cross-section is decreased with respect to its SM value until a pseudo-confidence level CL_s of 5% is obtained. The result is shown in Fig. 14 as an upper bound on the production cross-section, normalised to that in the SM, for masses of the Higgs boson from 0 to 110 GeV/c^2. The SM result described in the previous section corresponds to a ratio of 1.

9.4 Neutral Higgs bosons in the MSSM

The results in the hZ and hA channels reported in the previous sections are combined with the same statistical method as for the SM, also using earlier results at LEP2 energies [1,4,20,28]. The exclusion limits obtained at LEP1 [29] ($m_{\rm h}$>44 (46) GeV/c^2 when $m_{\rm h}$ is above (below) the AA threshold) are used as external constraints to limit the number of points in the scans.

9.4.1 The benchmark scenarios

At tree level, the production cross-sections and the Higgs branching fractions in the MSSM depend on two free parameters, $\tan\beta$ and one Higgs boson mass, or, alternatively, two Higgs boson masses, eg $m_{\rm A}$ and $m_{\rm h}$. Radiative corrections introduce additional parameters, related to supersymmetry breaking. Hereafter, we make the usual assumption that some of them are identical at a given energy scale: hence, the SU(2) and U(1) gaugino mass terms are assumed to be unified at the so-called GUT scale, while the sfermion mass terms or the squark trilinear couplings are assumed to be unified at the EW scale. Within these assumptions, the parameters beyond tree level are: the top quark mass, the Higgs mixing parameter, μ, the common sfermion mass term at the EW scale, M_{susy}, the SU(2) gaugino mass term at the EW scale, M_2, the gluino mass, $m_{\tilde{g}}$, and the common squark trilinear coupling at the EW scale, A. The U(1) gaugino mass term at the EW scale, M_1, is related to M_2 through the GUT relation $M_1 = (5/3)\tan^2\theta_W M_2$. The radiative corrections affect the relationships between the masses of the Higgs bosons, with the largest contributions arising from the top/stop loops. As an example, the h boson mass, which is below that of the Z boson at tree level, increases by a few tens of GeV/c^2 in some regions of the MSSM parameter space due to radiative corrections.

In the following, we consider three benchmark scenarios, as suggested in [30]. The first two schemes, called the $m_{\rm h}^{max}$ scenario and the no mixing scenario, rely on radiative corrections computed at two-loop order as in [31]. The values of the underlying parameters are quoted in Table 11. The two scenarios differ only by the value of $X_t = A - \mu\cot\beta$, the parameter which controls the mixing in the stop sector, and hence has the largest impact on the mass of the h boson. The $m_{\rm h}^{max}$ scenario leads to the maximum possible h mass as a function of $\tan\beta$. The no mixing scenario is its counterpart with vanishing mixing, leading to upper bounds on $m_{\rm h}$ which are at least 15 GeV/c^2 lower than in the $m_{\rm h}^{max}$ scheme.

The third scenario, called the large μ scenario, predicts at least one scalar Higgs boson with a mass within kinematic reach at LEP2 in each point of the MSSM parameter space. However, there are regions for which the Higgs bosons fall below detectability because of vanishing branching fractions into b quarks due to large radiative corrections. In this scenario, the radiative corrections are computed as in [32]. The values of the underlying parameters are given in Table 11. The main difference with the two previous schemes is the large and positive value of μ and the relatively small value of $m_{\tilde{g}}$.

9.4.2 The procedure

In the three benchmark scenarios, a scan is made over the MSSM parameters $\tan\beta$ and $m_{\rm A}$. The range in $m_{\rm A}$ spans from 12 GeV/c^2, the minimal value which has been searched for at LEP2 in the DELPHI analyses, up to the maximal value allowed by each scenario [30], that is up to M_{susy}, which is 1 TeV/c^2 in the $m_{\rm h}^{max}$ and no mixing schemes, and 400 GeV/c^2 in the large μ scenario (see Table 11). The range in $\tan\beta$ goes from the

minimal value allowed in each scenario (0.7 in the large μ scenario and 0.4 in the other two schemes) up to 50, a value chosen in the vicinity of the ratio of the top- and b-quark masses, which is an example of the large $\tan\beta$ hypothesis favored in some constrained MSSM models [33]. The scan steps are 1 GeV/c^2 in m_{A} and 0.1 in $\tan\beta$ in the regions where m_{h} varies rapidly with these parameters.

At each point of the parameter space, the hZ and hA cross-sections and the Higgs branching fractions are taken from theoretical databases provided by the LEP Higgs working group [34] on the basis of the theoretical calculations in [31,32]. The signal expectations in each channel are then derived from the theoretical cross-sections and branching fractions, the experimental luminosity and the efficiencies. A correction is applied to account for differing branching fractions of the Higgs bosons into $\mathrm{b\bar{b}}$ and $\tau^+\tau^-$ between the test point and the simulation (e.g. for the hZ process, the simulation is done in the SM framework). For the hA channels, to account for the difference between the masses of the h and A bosons at low $\tan\beta$ as well as for the non-negligible width of the h and A bosons at large $\tan\beta$, the set of efficiencies as a function of m_{A} obtained from the simulations at $\tan\beta = 50$ are applied above 30 in $\tan\beta$, while the efficiencies derived from the $\tan\beta = 20$ (or $\tan\beta = 2$) simulations are applied between 2.5 and 30 (or below 2.5) provided the difference between m_{h} and m_{A} at the test point is below 25 GeV/c^2; otherwise the set of efficiencies as a function of m_{h} and m_{A} derived from the additional simulations corresponding to large mass differences between the two bosons is preferred. The same holds for the discriminant information. Finally, as there is a large overlap in the backgrounds selected by the analyses in the $\mathrm{Hq\bar{q}}$ and 4b channels, only one channel is selected at each input point and at each centre-of-mass energy, on the basis of the best expected CL_s from background-only experiments. This ensures that the channels which are then combined in the global confidence level computations are independent.

9.4.3 Results

To illustrate the compatibility tests of data with background only and with signal plus background hypotheses in the hA channels, Fig. 15 shows the curves of the test-statistic $\mathcal{Q}$ and of the confidence levels CL_b and CL_s as a function of the test mass m_{h}+m_{A}, when using only the results in the two hA channels. The signal cross-sections are from the m_{h}^{max} scenario at $\tan\beta$ around 20. Over the whole range of test masses, data are in reasonable agreement with the background expectations. The largest deviation, slightly over one standard deviation, is observed for test masses m_{h}+m_{A} around 135 GeV/c^2 and is due to the small excess of events in the 4b channel with reconstructed masses in that region, as seen in Fig. 11.

Combining the results in the hZ and hA channels gives regions of the MSSM parameter space which are excluded at 95% CL or more. The excluded regions in the (m_{h}, $\tan\beta$), (m_{A}, $\tan\beta$) and (m_{h}, m_{A}) planes are presented in Fig. 16 for the m_{h}^{max} scenario and in Fig. 17 for the no mixing scenario. Basically, the exclusion is made by the results in the hZ (hA) channels in the low (large) $\tan\beta$ region while they both contribute at intermediate values. For m_{A} below the kinematic threshold $m_{\mathrm{h}} = 2m_{\mathrm{A}}$, which occurs at low $\tan\beta$ only, the decay $\mathrm{h}\rightarrow\mathrm{AA}$ opens, in which case it supplants the $\mathrm{h}\rightarrow\mathrm{b\bar{b}}$ decay. However, in most of the region, the $\mathrm{A}\rightarrow\mathrm{b\bar{b}}$ branching fraction remains large which explains why the results in the two ($\mathrm{h}\rightarrow\mathrm{AA}$) $\mathrm{q\bar{q}}$ channels reported in section 8.1, combined with studies of the $\mathrm{h}\rightarrow\mathrm{AA}$ decay at lower energies [4,20], exclude most of this region. An unexcluded hole remains in the no mixing scenario at $\tan\beta \sim 0.4$, m_{A} between 20 and 40 GeV/c^2 and m_{h} around 85 GeV/c^2 (visible only in the (m_{A}, $\tan\beta$) and (m_{h}, m_{A}) projections). In that

area, the A→c$\bar{\text{c}}$ decay dominates over the A→b$\bar{\text{b}}$ decay but the branching fractions in both modes are no longer large enough to give the necessary sensitivity for an exclusion.

The above results establish 95% CL lower limits on m_{h} and m_{A}, for either assumption on the mixing in the stop sector and for all values of $\tan\beta$ above 0.49:

$$m_{\mathrm{h}} > 85.9 \text{ GeV}/c^2 \qquad m_{\mathrm{A}} > 86.5 \text{ GeV}/c^2.$$

The expected median limits are 86.4 GeV/c^2 for m_{h} and 87.0 GeV/c^2 for m_{A}. The limit in m_{A} is reached in the no mixing scenario at $\tan\beta$ around 30 and thus is due to the non-negligible widths of the Higgs bosons, while the limit in m_{h} is obtained in the m_{h}^{max} scenario at $\tan\beta$ around 7, in a region where both the hZ and hA processes contribute. Furthermore, there are excluded ranges in $\tan\beta$ between 0.49 and 3.86 (expected [0.49-3.86]) in the no mixing case and between 0.65 and 1.75 (expected [0.72-1.75]) in the m_{h}^{max} scenario.

The excluded regions in the large μ scenario are presented in the (m_{h}, $\tan\beta$) and (m_{A}, $\tan\beta$) planes in Fig. 18. A large fraction of the allowed domain is excluded by the present results in the hZ and hA channels. In particular, given that the theoretical upper bound on the h boson mass in that scenario is slightly above 107 GeV/c^2, the sensitivity of the hZ channels is high even at large $\tan\beta$, which explains why the excluded region reaches the theoretically forbidden area for values of $\tan\beta$ up to 13.5. On the other hand, there is an unexcluded hole in the low $\tan\beta$ region at m_{h} around 60 GeV/c^2 which is due to a loss of sensitivity because of vanishing h→b$\bar{\text{b}}$ branching fractions in that region.

9.4.4 Extended scan of the parameter space

The robustness of the limits obtained in the benchmark scenarios has been tested in an extended scan of the MSSM parameter space. The Higgs bosons masses, cross-sections and branching fractions are computed with radiative corrections at two-loop order as in [31]. The top mass is fixed at 175 GeV/c^2 while the MSSM parameters, m_{A}, $\tan\beta$ and the parameters governing the radiative corrections, M_{susy}, M_2, μ and A are varied within the ranges given in Table 12. The values $\mu = \pm 1000$ GeV/c^2 have been studied in addition. As far as the granularity of the scan is concerned, steps of 1 GeV/c^2 are used for m_{A} up to 200 GeV/c^2 and larger steps between 200 and 1000 GeV/c^2; for each value of m_{A}, up to 2700 parameter combinations are investigated. To limit the number of points in the scan, only points above 70 GeV/c^2 in m_{h} and m_{A} are considered, since all points below this limit have already been excluded by our previous extended search [35]. The scan relies on the same channels and data sets as the representative scans previously reported and uses the same procedure to compute the confidence levels at each input point. However, for some parameter sets, the branching ratio of the neutral Higgs bosons into neutralinos is dominant, which is never the case in the benchmark scenarios. In such a case, the cross-section limits obtained in the search for invisible decays of a neutral Higgs boson [36] are applied to check whether these points are excluded or not. Any other point in a given plane (e.g. the (m_{h}, m_{A}) plane) is excluded if the observed CL_s at that point is below 5% for all sets of values of the parameters governing the radiative corrections that correspond to that point. The results of this extended scan are presented in Fig. 19 in the three projections (m_{h}, $\tan\beta$), (m_{A}, $\tan\beta$) and (m_{h}, m_{A}). The extension of the MSSM parameter ranges in the scan leads to 95% CL lower limits of 85 GeV/c^2 on m_{h} and 86 GeV/c^2 on m_{A}, thus only about 1 GeV/c^2 below the limits obtained in the m_{h}^{max} and no mixing scenarios.

10 Conclusions

The 228 pb^{-1} of data taken by DELPHI at 191.6-201.7 GeV, combined with our lower energy data, sets the lower limit at 95% CL on the mass of the Standard Model Higgs boson at:

$$m_{\mathrm{H}} > 107.3 \text{ GeV}/c^2.$$

These data sets also allow studies of the representative m_{h}^{max} and no mixing scenarios. The 95% CL limits on the masses of the lightest neutral scalar and neutral pseudoscalar are:

$$m_{\mathrm{h}} > 85.9 \text{ GeV}/c^2 \qquad m_{\mathrm{A}} > 86.5 \text{ GeV}/c^2.$$

for all values of $\tan\beta$ above 0.49 and assuming $m_{\mathrm{A}} > 12$ GeV/c^2. These limits have been proved to be robust in an extended scan of the MSSM parameter space.

Acknowledgements

We are greatly indebted to our technical collaborators, to the members of the CERN-SL Division for the excellent performance of the LEP collider, and to the funding agencies for their support in building and operating the DELPHI detector.
We acknowledge in particular the support of
Austrian Federal Ministry of Science and Traffics, GZ 616.364/2-III/2a/98,
FNRS–FWO, Flanders Institute to encourage scientific and technological research in the industry (IWT), Belgium,
FINEP, CNPq, CAPES, FUJB and FAPERJ, Brazil,
Czech Ministry of Industry and Trade, GA CR 202/96/0450 and GA AVCR A1010521,
Danish Natural Research Council,
Commission of the European Communities (DG XII),
Direction des Sciences de la Matière, CEA, France,
Bundesministerium für Bildung, Wissenschaft, Forschung und Technologie, Germany,
General Secretariat for Research and Technology, Greece,
National Science Foundation (NWO) and Foundation for Research on Matter (FOM), The Netherlands,
Norwegian Research Council,
State Committee for Scientific Research, Poland, 2P03B06015, 2P03B11116 and SPUB/P03/DZ3/99,
JNICT–Junta Nacional de Investigação Científica e Tecnológica, Portugal,
Vedecka grantova agentura MS SR, Slovakia, Nr. 95/5195/134,
Ministry of Science and Technology of the Republic of Slovenia,
CICYT, Spain, AEN96–1661 and AEN96-1681,
The Swedish Natural Science Research Council,
Particle Physics and Astronomy Research Council, UK,
Department of Energy, USA, DE–FG02–94ER40817,

References

[1] DELPHI Collaboration, P. Abreu et al., E. Phys. J. **C17** (2000) 187/549.

[2] ALEPH Collaboration, CERN EP/2000-019, subm. to E. Phys. J.
L3 Collaboration, Phys. Lett. **B461** (1999) 376 and Phys. Lett. **B471** (1999) 321.
OPAL Collaboration E. Phys. J. **C12** (2000) 567.

[3] DELPHI Collaboration, P. Abreu et al., Phys. Lett. **B499** (2001) 23.

[4] DELPHI Collaboration, P. Abreu et al., E. Phys. J. **C10** (1999) 563.

[5] DELPHI Collaboration, P. Aarnio et al., Nucl. Instr. Meth. **303** (1991) 233.

[6] DELPHI Collaboration, P. Abreu et al., Nucl. Instr. Meth. **A378** (1996) 57.

[7] DELPHI Silicon Tracker Group, P.Choduba et al., Nucl. Instr. Meth. **A412** (1998) 304.

[8] T. Sjöstrand, Comp. Phys. Comm. **39** (1986) 347. Version 6.125 was used.

[9] S. Jadach, B.F.L. Ward and Z. Was, Comp. Phys. Comm. **124** (2000) 23 and **79** (1994) 503.

[10] F.A. Berends, R. Pittau and R. Kleiss, Comp. Phys. Comm. **85** (1995) 437.

[11] J. Fujimoto et al., Comp. Phys. Comm. **100** (1997) 128.

[12] S. Jadach, W. Placzek, M. Skrzypek, B.F.L. Ward and Z. Was, Comp. Phys. Comm. **119** (1999) 272.

[13] S. Nova, A. Olchevski and T. Todorov, in CERN Report 96-01, Vol. 2, p. 224 (1996).

[14] F.A. Berends, P.H. Daverveldt and R. Kleiss, Nucl. Phys. **B253** (1985) 421; Comp. Phys. Comm. **40** (1986) 271, 285 and 309.

[15] S. Jadach, W. Placzek and B.F.L. Ward, Phys. Lett. **B390** (1997) 298.

[16] P. Janot, in CERN Report 96-01, Vol. 2, p. 309 (1996); version 3 released in December 1999, `http://alephwww.cern.ch/janot/Generators.html`.

[17] Physics at LEP2, ed. G. Altarelli, T. Sjöstrand and F. Zwirner, CERN Report 96-01, Vol. 1, p. 363.

[18] G. Borisov, Nucl. Instr. Meth. **A417** (1998) 384.

[19] DELPHI Collaboration, P. Abreu et al., Eur. Phys. J. **C10** (1999) 415.

[20] DELPHI Collaboration, P. Abreu et al., Eur. Phys. J. **C2** (1998) 1.

[21] DELPHI Collaboration, P. Abreu et al., Eur. Phys. J. **C2** (1998) 581 (Sect. 5.2.)

[22] P. Abreu et al., Nucl. Instr. Meth. **A427** (1999) 487.

[23] A.L. Read, in CERN Report 2000-005, p. 81 (2000).

[24] C. Peterson, T. Rognvaldsson and L. Lonnblad, Comp. Phys. Comm. **81** (1994) 185.

[25] DELPHI Collaboration, P. Abreu et al., Phys. Lett **B462** (1999) 410.

[26] J. Schwindling, B. Mansoulié and O. Couet, 'Using Multi-Layer Perceptrons in PAW', PAW manual, `http://wwwinfo.cern.ch/asd/paw/mlpfit/pawmlp.html`

[27] DELPHI Collaboration, P. Abreu et al., Nucl. Phys. **B342** (1990) 1.
DELPHI Collaboration, P. Abreu et al., Zeit. Phys. **C51** (1991) 25.
DELPHI Collaboration, P. Abreu et al., Nucl. Phys. **B373** (1992) 3.
DELPHI Collaboration, P. Abreu et al., Nucl. Phys. **B421** (1994) 3.

[28] DELPHI Collaboration, P. Abreu et al., Zeit. Phys. **C73** (1996) 1.

[29] G.Wormser, in proc. of the XXVI ICHEP conference (Dallas, August 1992), Vol. 2, pages 1309-14. See ref. 4.
DELPHI Collaboration, P. Abreu et al., Zeit. Phys. **C67** (1995) 69.

[30] M. Carena, S. Heinemeyer, C. Wagner and G. Weiglein, *Suggestions for improved benchmark scenarios for Higgs boson searches at LEP2* CERN-TH/99-374, DESY 99-186 or hep-ph/9912223.
M. Carena, H.E. Haber, S. Heinemeyer, W. Hollik, C.E.M. Wagner and G. Weiglein,

Nucl. Phys. **B580** (2000) 29.
[31] S. Heinemeyer, W. Hollik and G. Weiglein, Eur. Phys. J. **C9** (1999) 343;
[32] M. Carena, M. Quiros and C.E.M. Wagner, Nucl. Phys. **B461** (1996) 407 and Phys. Rev. **D62** (2000) 055008.
[33] M. Carena, S. Pokorski and C.E.M. Wagner, Nucl. Phys. **B406** (1993) 59.
[34] ALEPH, DELPHI, L3, OPAL Collaborations and the LEP Higgs working group, CERN-EP/2000-055.
[35] DELPHI Collaboration, P. Abreu et al., E. Phys. J. **C17** (2000) 549.
[36] DELPHI Collaboration, P. Abreu et al., CERN-EP/2000-051.

Selection	Data	Total background	$q\bar{q}(\gamma)$	4 fermion	Efficiency (%)
Electron channel 25.2 pb^{-1}					
Preselection	152	158.6± 2.5	111.7	43.6	81.0
cuts on leptons	15	9.7± 0.6	2.5	6.2	65.7
5C fit prob.	3	3.7± 0.3	1.1	2.3	61.7
final selection	1	1.19± 0.08	0.05	1.1	55.0
Muon channel 25.9 pb^{-1}					
Preselection	336	364.8 ± 3.8	274.5	86.7	78.8
cuts on leptons	2	2.30 ± 0.12	0.15	2.15	72.4
final selection	1	0.93 ± 0.02	0.0	0.93	57.8
Tau channel 25.9 pb^{-1}					
Preselection	1209	1127± 2.6	747	380	98.3
$\ell^+\ell^-q\bar{q}$	0	2.1± 0.1	0.09	2.0	18.5
final selection	0	0.76±0.08	0.04	0.72	16.7
Missing energy channel 24.9 pb^{-1}					
Anti $\gamma\gamma$	2378	2368.0± 4.5	1904.1	427.3	86.0
Preselection	139	130.7 ± 2.0	81.3	45.7	73.9
$\mathcal{L}>1.0$	11	12.6± 0.6	7.7	4.9	59.8
Four-jet channel 25.9 pb^{-1}					
Preselection	302	280.6± 2.8	91.8	188.8	89.4
ANN > 0.3	16	19.1± 0.5	4.3	14.8	60.4
hA four-jet channel 25.9 pb^{-1}					
Preselection	273	255.1± 2.3	79.7	175.4	90.7
$\mathcal{L}>0.1$	18	16.8 ± 0.6	7.7	9.1	85.0

Table 1: Effect of the selection cuts on data, simulated background and simulated signal events at $\sqrt{s} = 191.6$ GeV. Efficiencies are given for a signal with $m_{\mathrm{H}} = 105$ GeV/c^2 for the SM and m_{A}= 85 GeV/c^2, $\tan\beta = 20$ for the MSSM. The quoted errors are statistical only. For each channel, the first line shows the integrated luminosity used; the last line gives the inputs for the limit derivation.

Selection	Data	Total background	$q\bar{q}(\gamma)$	4 fermion	Efficiency (%)
Electron channel 76.2 pb^{-1}					
Preselection	452	428.8± 3.5	284.7	133.7	79.1
cuts on leptons	33	29.0± 1.3	7.7	18.5	64.2
5C fit prob.	18	11.5± 0.7	3.15	7.5	60.6
final selection	5	3.88±0.18	0.13	3.5	57.4
Muon channel 76.9 pb^{-1}					
Preselection	1081	1092.5 ± 4.2	801.5	280.2	79.5
cuts on leptons	3	7.19 ± 0.17	0.46	6.73	71.4
final selection	2	3.02 ± 0.07	0.02	3.0	67.4
Tau channel 76.9 pb^{-1}					
Preselection	3479	3215 ± 4.7	2056	1159	98.3
$\ell^+\ell^- q\bar{q}$	7	6.6± 0.2	0.5	6.1	18.5
final selection	3	2.38±0.12	0.07	2.31	18.3
Missing energy channel 75.0 pb^{-1}					
Anti $\gamma\gamma$	7005	6757.8 ± 5.2	5343.0	1309.1	86.1
Preselection	403	384.7 ± 2.2	238.8	134.1	74.4
$\mathcal{L}>$ 1.0	38	34.0 ± 0.6	20.2	13.8	62.1
Four-jet channel 76.9 pb^{-1}					
Preselection	839	827.1± 5.1	260.0	567.1	87.5
ANN $>$ 0.3	51	58.7± 0.7	11.3	47.1	67.7
hA four-jet channel 76.9 pb^{-1}					
Preselection	747	757.3± 4.7	232.3	525.0	90.9
$\mathcal{L}>$ 0.1	47	48.0± 0.7	19.6	28.5	86.8

Table 2: As in Table 1, but for $\sqrt{s}$ = 195.6 GeV.

Selection	Data	Total background	$q\bar{q}(\gamma)$	4 fermion	Efficiency (%)
Electron channel 82.8 pb^{-1}					
Preselection	489	453.3± 3.6	294.5	148.4	79.3
cuts on leptons	30	31.1± 1.4	7.0	21.3	63.3
5C fit prob.	11	12.8±1.1	2.6	8.4	59.5
final selection	4	4.22±0.19	0.05	3.9	56.0
Muon channel 84.3 pb^{-1}					
Preselection	1141	1148.4 ± 4.3	807.3	329.8	78.9
cuts on leptons	11	8.20 ± 0.21	0.54	7.66	72.1
final selection	5	3.59 ± 0.08	0.02	3.57	69.7
Tau channel 84.3 pb^{-1}					
Preselection	3629	3434 ± 9.7	2152	1282	98.1
$\ell^+\ell^- q\bar{q}$	8	7.7± 0.2	0.5	7.2	18.9
final selection	3	2.60±0.13	0.14	2.46	17.9
Missing energy channel 82.2 pb^{-1}					
Anti $\gamma\gamma$	7211	7112.4± 5.8	5566.8	1450.8	85.5
Preselection	421	425.7 ± 2.5	260.6	151.8	75.8
$\mathcal{L}> 1.0$	38	40.5± 0.7	24.4	16.1	64.0
Four-jet channel 84.3 pb^{-1}					
Preselection	882	896.8± 2.9	273.6	623.3	87.7
ANN > 0.3	61	65.3± 0.8	13.1	52.2	70.4
hA four-jet channel 84.3 pb^{-1}					
Preselection	783	817.9± 2.7	243.1	574.8	90.9
$\mathcal{L}> 0.1$	44	49.1± 0.7	18.9	30.2	85.5

Table 3: As in Table 1, but for $\sqrt{s} = 199.6$ GeV.

Selection	Data	Total background	$q\bar{q}(\gamma)$	4 fermion	Efficiency (%)
Electron channel 40.4 pb^{-1}					
Preselection	232	214.3± 2.0	136.5	72.7	79.6
cuts on leptons	18	15.7± 0.7	3.83	10.6	64.3
5C fit prob.	3	6.47± 0.55	1.51	4.1	60.2
final selection	1	2.18±0.10	0.09	1.97	56.8
Muon channel 41.1 pb^{-1}					
Preselection	574	561.9 ± 2.9	391.1	165.2	81.0
cuts on leptons	0	4.31 ± 0.14	0.28	4.03	73.5
final selection	0	1.83 ± 0.04	0.0	1.83	71.0
Tau channel 41.1 pb^{-1}					
Preselection	1716	1648± 5.8	1019	629	98.5
$\ell^+\ell^- q\bar{q}$	0	3.6± 0.1	0.2	3.4	23.1
final selection	0	1.17± 0.05	0.03	1.14	22.1
Missing energy channel 40.4 pb^{-1}					
Anti $\gamma\gamma$	3305	3401.1 ± 3.7	2632.3	715.3	85.8
Preselection	209	204.9 ± 1.7	125.2	73.3	77.8
$\mathcal{L}>$ 1.0	21	18.6 ± 0.5	11.0	7.5	65.7
Four-jet channel 41.1 pb^{-1}					
Preselection	442	432.4± 3.2	129.8	302.6	87.0
ANN $>$ 0.3	33	32.3± 0.5	6.5	25.8	69.7
hA four-jet channel 41.1 pb^{-1}					
Preselection	405	393.9± 2.1	115.6	278.3	90.4
$\mathcal{L}>$ 0.1	27	23.9± 0.4	8.9	14.9	84.6

Table 4: As in Table 1, but for $\sqrt{s} = 201.7$ GeV.

m_{H} (GeV/c^2)	Electron channel	Muon channel	$\mathrm{H}\tau^+\tau^-$ channel	$\tau^+\tau^-\mathrm{Z}$ channel	Mis. Energy channel	Four-jet channel
$\sqrt{s} = 191.6$ GeV						
70.0	56.1 ± 1.1	65.0 ± 1.1	21.6 ± 0.9	22.5 ± 0.9	49.0 ± 1.1	45.1 ± 1.1
80.0	57.4 ± 1.1	70.6 ± 1.0	19.6 ± 0.9	24.0 ± 1.0	57.0 ± 1.1	57.5 ± 1.1
85.0	59.4 ± 0.8	68.8 ± 1.0	19.6 ± 0.9	23.3 ± 0.9	61.9 ± 1.1	62.3 ± 1.1
90.0	58.4 ± 0.8	69.0 ± 1.0	20.6 ± 0.9	22.8 ± 0.9	65.0 ± 1.1	69.1 ± 1.0
95.0	58.1 ± 0.8	70.0 ± 0.8	19.8 ± 0.9	22.0 ± 0.9	66.5 ± 1.1	69.1 ± 1.0
100.0	55.2 ± 0.8	67.4 ± 1.0	19.5 ± 0.9	19.9 ± 0.9	61.9 ± 1.1	69.4 ± 1.0
105.0	55.0 ± 0.8	57.8 ± 1.1	16.7 ± 0.8	19.3 ± 0.9	59.8 ± 1.1	60.5 ± 1.1
110.0	52.5 ± 1.1	47.4 ± 1.1	14.0 ± 0.8	18.4 ± 0.9	59.1 ± 1.1	53.7 ± 1.1
$\sqrt{s} = 195.6$ GeV						
70.0	53.9 ± 1.1	63.3 ± 1.1	20.0 ± 0.9	23.0 ± 0.9	47.9 ± 1.1	42.7 ± 1.1
80.0	58.3 ± 1.1	68.3 ± 1.0	22.3 ± 0.9	21.8 ± 0.9	55.3 ± 1.1	56.4 ± 1.1
85.0	59.8 ± 1.1	71.1 ± 1.0	21.3 ± 1.3	24.4 ± 1.4	60.8 ± 1.1	60.4 ± 1.1
90.0	57.9 ± 1.1	67.7 ± 1.1	20.8 ± 1.3	23.6 ± 1.3	64.2 ± 1.1	66.1 ± 1.0
95.0	59.8 ± 1.1	69.7 ± 1.1	21.3 ± 1.3	23.4 ± 1.3	67.8 ± 1.0	68.5 ± 1.0
100.0	59.0 ± 0.9	71.3 ± 0.8	18.2 ± 1.2	21.8 ± 1.3	65.8 ± 0.7	70.0 ± 0.6
105.0	57.4 ± 1.1	67.4 ± 1.1	18.3 ± 1.2	20.2 ± 1.3	62.1 ± 1.1	67.7 ± 1.0
110.0	56.0 ± 1.1	55.5 ± 1.1	14.4 ± 0.8	20.4 ± 0.9	55.6 ± 1.1	57.3 ± 1.1
115.0	53.5 ± 1.1	45.9 ± 1.1	13.8 ± 0.8	16.9 ± 0.8	53.2 ± 1.1	52.4 ± 1.1
$\sqrt{s} = 199.6$ GeV						
70.0	54.6 ± 1.1	62.5 ± 1.1	20.0 ± 0.9	23.3 ± 0.9	44.9 ± 1.1	44.2 ± 1.1
80.0	56.9 ± 1.1	68.1 ± 1.0	20.7 ± 0.9	23.6 ± 0.9	52.5 ± 1.1	55.1 ± 1.1
85.0	55.8 ± 1.6	70.2 ± 1.0	22.0 ± 1.5	23.6 ± 1.5	59.5 ± 1.1	59.5 ± 1.1
90.0	59.6 ± 1.1	69.5 ± 1.0	19.2 ± 1.4	23.9 ± 1.5	62.2 ± 1.1	63.6 ± 1.0
95.0	59.6 ± 1.1	70.9 ± 1.1	19.9 ± 1.4	21.7 ± 1.5	64.7 ± 1.1	67.3 ± 1.0
100.0	57.9 ± 1.1	72.1 ± 1.0	20.0 ± 1.4	22.1 ± 1.5	67.7 ± 1.0	69.0 ± 1.0
105.0	56.0 ± 0.9	69.7 ± 0.6	17.9 ± 1.4	19.5 ± 1.4	64.0 ± 1.0	70.4 ± 0.6
110.0	56.1 ± 1.1	66.7 ± 1.0	18.3 ± 1.4	20.7 ± 1.4	61.7 ± 0.8	68.2 ± 1.0
115.0	53.5 ± 1.1	58.3 ± 1.2	14.4 ± 1.1	18.8 ± 1.2	60.4 ± 0.9	60.2 ± 1.5
$\sqrt{s} = 201.7$ GeV						
70.0	53.9 ± 1.1	62.5 ± 1.1	19.6 ± 0.9	24.2 ± 1.0	41.2 ± 1.1	42.5 ± 1.1
80.0	57.1 ± 1.1	67.2 ± 1.0	19.1 ± 0.9	24.2 ± 1.0	50.5 ± 1.1	53.0 ± 1.1
85.0	61.4 ± 1.1	69.5 ± 1.1	22.0 ± 1.3	23.6 ± 1.3	59.1 ± 1.1	58.5 ± 1.1
90.0	58.6 ± 1.1	68.3 ± 1.1	23.0 ± 1.3	23.2 ± 1.3	61.9 ± 1.1	64.5 ± 1.1
95.0	60.2 ± 1.1	70.0 ± 1.1	21.2 ± 1.3	21.4 ± 1.3	64.3 ± 1.1	63.1 ± 1.1
100.0	60.2 ± 1.1	67.5 ± 1.1	21.7 ± 1.2	22.0 ± 1.3	66.9 ± 1.0	69.9 ± 1.0
105.0	56.8 ± 0.9	71.0 ± 1.0	22.1 ± 1.2	22.8 ± 1.3	65.7 ± 1.1	69.7 ± 1.1
110.0	56.9 ± 1.1	69.1 ± 1.0	15.0 ± 1.1	19.3 ± 1.2	62.1 ± 1.1	69.4 ± 1.0
115.0	57.3 ± 1.1	58.3 ± 1.2	14.7 ± 1.1	18.8 ± 1.2	63.4 ± 1.1	61.6 ± 1.1

Table 5: HZ channels: efficiencies (in %) of the selection at $\sqrt{s} = 191.6$-201.7 GeV as a function of the mass of the Higgs boson, for masses above 70 GeV/c^2. The quoted errors are statistical only.

m_{H}	$\sqrt{s}$ (GeV)			
(GeV/c^2)	191.6	195.6	199.6	201.7
Electron channel				
50.0	5.8 ± 0.5	8.5 ± 0.6	8.8 ± 0.6	8.8 ± 0.6
60.0	37.0 ± 1.1	37.0 ± 1.1	36.2 ± 1.1	38.6 ± 1.1
Muon channel				
40.0	27.8 ± 1.0	25.0 ± 1.0	23.2 ± 0.9	23.4 ± 0.9
50.0	44.4 ± 1.1	41.6 ± 1.1	38.4 ± 1.1	37.4 ± 1.1
60.0	55.0 ± 1.1	55.2 ± 1.1	52.8 ± 1.1	49.4 ± 1.1
H$\tau^+\tau^-$channel				
50.0	12.5 ± 0.7	11.9 ± 0.7	12.7 ± 0.7	12.6 ± 0.7
60.0	18.9 ± 0.9	18.4 ± 0.9	18.8 ± 0.9	19.1 ± 0.9
$\tau^+\tau^-$Z channel				
50.0	7.9 ± 0.6	6.0 ± 0.5	6.3 ± 0.5	6.0 ± 0.5
60.0	21.2 ± 0.9	17.3 ± 0.8	14.1 ± 0.8	14.1 ± 0.8
Missing Energy channel				
12.0	17.6 ± 0.8	21.7 ± 0.9	25.2 ± 1.0	18.1 ± 0.9
18.0	23.8 ± 0.9	32.8 ± 1.0	34.4 ± 1.1	22.4 ± 0.9
24.0	25.3 ± 0.9	32.9 ± 1.0	33.7 ± 1.1	22.2 ± 0.9
30.0	25.6 ± 1.0	32.8 ± 1.0	31.5 ± 1.0	23.5 ± 0.9
40.0	29.0 ± 1.0	32.0 ± 1.0	32.0 ± 1.0	23.3 ± 0.9
50.0	33.5 ± 1.0	35.7 ± 1.1	34.0 ± 1.1	28.5 ± 1.0
60.0	36.0 ± 1.1	41.7 ± 1.1	38.1 ± 1.1	35.5 ± 1.1
Four-jet channel				
24.0	6.8 ± 0.6	8.0 ± 0.6	7.9 ± 0.6	8.6 ± 0.7
30.0	13.5 ± 0.8	16.2 ± 0.8	16.6 ± 0.8	17.1 ± 0.8
40.0	29.8 ± 1.0	29.6 ± 1.0	28.1 ± 1.0	28.9 ± 1.0
50.0	38.6 ± 1.1	39.6 ± 1.1	37.8 ± 1.1	38.8 ± 1.0
60.0	42.9 ± 1.1	44.0 ± 1.1	42.4 ± 1.1	42.1 ± 1.1

Table 6: HZ channels: efficiencies (in %) of the selection at $\sqrt{s}$ = 191.6-201.7 GeV as a function of the mass of the Higgs boson, for masses below 70 GeV/c^2. Only efficiencies higher than 5% are shown. The quoted errors are statistical only.

		A→bb	A→c$\bar{\text{c}}$
m_{A} (GeV/c^2)	m_{h} (GeV/c^2)	Efficiency (%)	Efficiency (%)
12.0	30.0	20.8 ± 1.2	6.5 ± 0.8
12.0	50.0	48.5 ± 1.6	19.2 ± 1.2
12.0	70.0	56.0 ± 1.6	24.4 ± 1.4
12.0	90.0	80.2 ± 1.3	37.6 ± 1.5
12.0	105.0	77.3 ± 1.3	54.3 ± 1.6
20.0	50.0	46.0 ± 1.6	17.4 ± 1.2
20.0	70.0	57.6 ± 1.6	24.3 ± 1.3
20.0	90.0	75.6 ± 1.4	36.4 ± 1.5
20.0	105.0	80.1 ± 1.3	59.5 ± 1.5
30.0	70.0	63.4 ± 1.6	26.0 ± 1.4
30.0	90.0	72.8 ± 1.5	31.8 ± 1.5
30.0	105.0	81.4 ± 1.3	55.6 ± 1.6
40.0	90.0	74.3 ± 1.5	35.0 ± 1.6
40.0	105.0	80.3 ± 1.3	42.4 ± 1.6
50.0	105.0	82.4 ± 1.3	47.8 ± 1.7

Table 7: (h → AA)(Z → q$\bar{\text{q}}$) channels with A→b$\bar{\text{b}}$ or A→c$\bar{\text{c}}$: efficiencies of the selection (in %) at $\sqrt{s} = 199.6$ GeV as a function of the masses of the A and h bosons. The quoted errors are statistical only.

	$\tan\beta = 2$		$\tan\beta = 20$		$\tan\beta = 50$	
m_{A}	Four-jet	Tau	Four-jet	Tau	Four-jet	Tau
(GeV/c^2)	channel	channel	channel	channel	channel	channel
$\sqrt{s} = 191.6$ GeV						
40.0	39.9 ± 1.1	-	21.8 ± 0.9	-	14.5 ± 0.8	-
50.0	58.3 ± 1.1	-	54.8 ± 1.1	-	49.5 ± 1.1	-
60.0	66.1 ± 1.0	7.1 ± 0.6	67.3 ± 1.0	6.2 ± 0.5	63.6 ± 1.1	6.5 ± 0.5
70.0	72.4 ± 1.0	14.6 ± 0.8	75.2 ± 1.0	22.7 ± 0.9	73.4 ± 1.0	16.9 ± 0.8
80.0	77.1 ± 0.9	22.3 ± 0.9	81.1 ± 0.9	24.3 ± 1.0	77.0 ± 0.9	19.9 ± 0.9
85.0	78.8 ± 0.9	23.4 ± 0.9	85.0 ± 0.8	24.1 ± 0.9	80.8 ± 0.9	20.7 ± 0.9
90.0	83.1 ± 0.8	22.6 ± 0.9	82.8 ± 0.8	22.1 ± 0.9	79.0 ± 0.9	19.7 ± 0.9
95.0	82.2 ± 0.8	20.6 ± 0.9	78.5 ± 0.9	19.0 ± 0.9	77.4 ± 1.0	15.4 ± 0.8
$\sqrt{s} = 195.6$ GeV						
40.0	38.4 ± 1.1	-	17.7 ± 0.8	-	13.6 ± 0.8	-
50.0	58.0 ± 1.1	-	55.4 ± 1.1	-	47.1 ± 1.1	-
60.0	67.0 ± 1.0	7.0 ± 0.6	66.9 ± 1.0	7.2 ± 0.6	62.0 ± 1.1	6.0 ± 0.5
70.0	71.1 ± 1.1	13.4 ± 0.8	72.6 ± 1.0	21.4 ± 0.9	71.3 ± 1.0	17.5 ± 0.8
80.0	81.0 ± 0.8	15.9 ± 1.1	83.9 ± 0.8	20.3 ± 1.3	77.4 ± 0.9	23.7 ± 0.9
85.0	81.9 ± 0.8	22.2 ± 1.3	86.8 ± 0.8	21.8 ± 1.3	80.9 ± 0.9	21.1 ± 0.9
90.0	81.5 ± 0.8	25.3 ± 1.4	87.0 ± 0.6	22.1 ± 1.3	82.0 ± 0.9	20.1 ± 0.9
95.0	82.6 ± 0.8	20.6 ± 0.9	82.5 ± 0.8	19.0 ± 0.9	81.2 ± 0.9	17.6 ± 0.8
$\sqrt{s} = 199.6$ GeV						
40.0	38.6 ± 1.1	-	14.5 ± 0.8	-	11.2 ± 0.7	-
50.0	58.3 ± 1.1	-	54.8 ± 1.1	-	47.7 ± 1.1	-
60.0	67.0 ± 1.0	5.8 ± 0.5	66.9 ± 1.0	6.8 ± 0.6	62.0 ± 1.1	5.5 ± 0.5
70.0	71.1 ± 1.1	11.4 ± 0.7	72.6 ± 1.0	19.1 ± 0.9	71.3 ± 1.0	15.1 ± 0.8
80.0	78.4 ± 0.9	15.9 ± 1.1	82.2 ± 0.9	22.5 ± 1.3	77.4 ± 0.9	20.1 ± 0.9
85.0	80.2 ± 0.8	20.8 ± 1.3	85.5 ± 0.8	25.6 ± 1.4	80.9 ± 0.9	20.6 ± 0.9
90.0	83.5 ± 0.8	24.4 ± 1.4	85.6 ± 0.8	21.6 ± 1.3	82.0 ± 0.9	21.1 ± 0.9
95.0	84.5 ± 0.7	20.6 ± 1.3	83.5 ± 0.8	22.7 ± 1.3	81.2 ± 0.9	18.9 ± 0.9
$\sqrt{s} = 201.7$ GeV						
40.0	33.3 ± 1.0	-	13.6 ± 0.8	-	10.5 ± 0.7	-
50.0	60.1 ± 1.1	-	54.6 ± 1.1	-	47.1 ± 1.1	-
60.0	67.0 ± 1.0	5.8 ± 0.5	66.9 ± 1.0	6.7 ± 0.6	62.0 ± 1.1	5.8 ± 0.5
70.0	71.1 ± 1.1	11.2 ± 0.7	72.6 ± 1.0	17.0 ± 0.8	71.3 ± 1.0	15.4 ± 0.8
80.0	77.0 ± 0.9	15.9 ± 1.1	80.4 ± 0.9	22.5 ± 1.3	77.4 ± 0.9	20.5 ± 0.9
85.0	80.2 ± 0.8	20.8 ± 1.3	84.6 ± 0.8	25.6 ± 1.4	80.9 ± 0.9	22.4 ± 0.9
90.0	82.5 ± 0.8	24.4 ± 1.4	86.8 ± 0.8	21.6 ± 1.3	82.0 ± 0.9	20.8 ± 0.9
95.0	85.8 ± 0.8	20.6 ± 1.3	84.1 ± 0.8	22.7 ± 1.3	81.2 ± 0.9	18.4 ± 0.9

Table 8: hA channels: efficiencies of the selection (in %) at $\sqrt{s} = 191.6$-201.7 GeV as a function of the mass of the A boson and $\tan\beta$. Only efficiencies higher than 5% are shown. The quoted errors are statistical only.

$m_{\rm A}$ (GeV/c^2)	$m_{\rm h}$ (GeV/c^2)	Efficiency (%)	$m_{\rm A}$ (GeV/c^2)	$m_{\rm h}$ (GeV/c^2)	Efficiency (%)
12.0	70.0	27.2 ± 1.4	30.0	130.0	67.7 ± 1.5
12.0	90.0	35.8 ± 1.5	30.0	150.0	60.1 ± 1.5
12.0	110.0	59.8 ± 1.5	50.0	70.0	66.2 ± 1.5
12.0	130.0	63.4 ± 1.5	50.0	90.0	78.4 ± 1.3
12.0	150.0	52.0 ± 1.6	50.0	110.0	80.5 ± 1.3
12.0	170.0	32.4 ± 1.5	50.0	130.0	75.5 ± 1.4
30.0	50.0	19.9 ± 1.3	70.0	90.0	80.4 ± 1.3
30.0	70.0	54.7 ± 1.6	70.0	110.0	81.8 ± 1.2
30.0	90.0	65.2 ± 1.5	80.0	90.0	87.2 ± 1.1
30.0	110.0	68.9 ± 1.5	85.0	95.0	83.5 ± 1.2

Table 9: hA four-jet channel : efficiencies of the selection (in %) at $\sqrt{s} = 199.6$ GeV as a function of the masses of the A and h bosons, from simulated samples corresponding to large mass differences between the two bosons. The quoted errors are statistical only.

$\sqrt{s}$	HZ channel			hA channel		
(GeV)	Data	Background	Signal	Data	Background	Signal
191.6	1	4.8±0.3	0.16±0.01	3	1.1±0.2	0.56±0.02
195.6	13	12.4±0.3	1.18±0.02	1	2.9±0.2	2.00±0.04
199.6	13	12.9±0.3	4.70±0.06	3	2.9±0.2	2.31±0.05
201.7	5	6.9±0.2	2.87±0.06	1	1.5±0.1	1.24±0.02

Table 10: Observed and expected rates after tight selections applied to data at $\sqrt{s} = 191.6$-201.7 GeV. Signal expectations are given for a signal with $m_{\rm H} = 105$ GeV/c^2 for the SM and $m_{\rm A}$= 85 GeV/c^2, $\tan\beta = 20$ for the MSSM. The quoted errors are statistical only.

scenario	$m_{\rm top}$ (GeV/c^2)	M_{susy} (GeV/c^2)	M_2 (GeV/c^2)	$m_{\tilde{g}}$ (GeV/c^2)	μ (GeV/c^2)	$X_t = A - \mu\cot\beta$ (GeV/c^2)
$m_{\rm h}^{max}$ scenario	174.3	1000	200	800	-200	2 M_{susy}
no mixing	174.3	1000	200	800	-200	0
large μ	174.3	400	400	200	1000	-300

Table 11: Values of the underlying parameters for the three representative MSSM scenarios scanned in this paper.

Parameter	$m_{\rm A}$ (GeV/c^2)	$\tan\beta$	M_{susy} (GeV/c^2)	M_2 (GeV/c^2)	μ (GeV/c^2)	A/M_{susy}
Range	20 : 1000	0.5 : 50	200 : 1000	200 : 1000	−500 : +500	−2 : +2

Table 12: Ranges of variation of the underlying parameters used in the extended scan of the MSSM parameter space described in this paper.

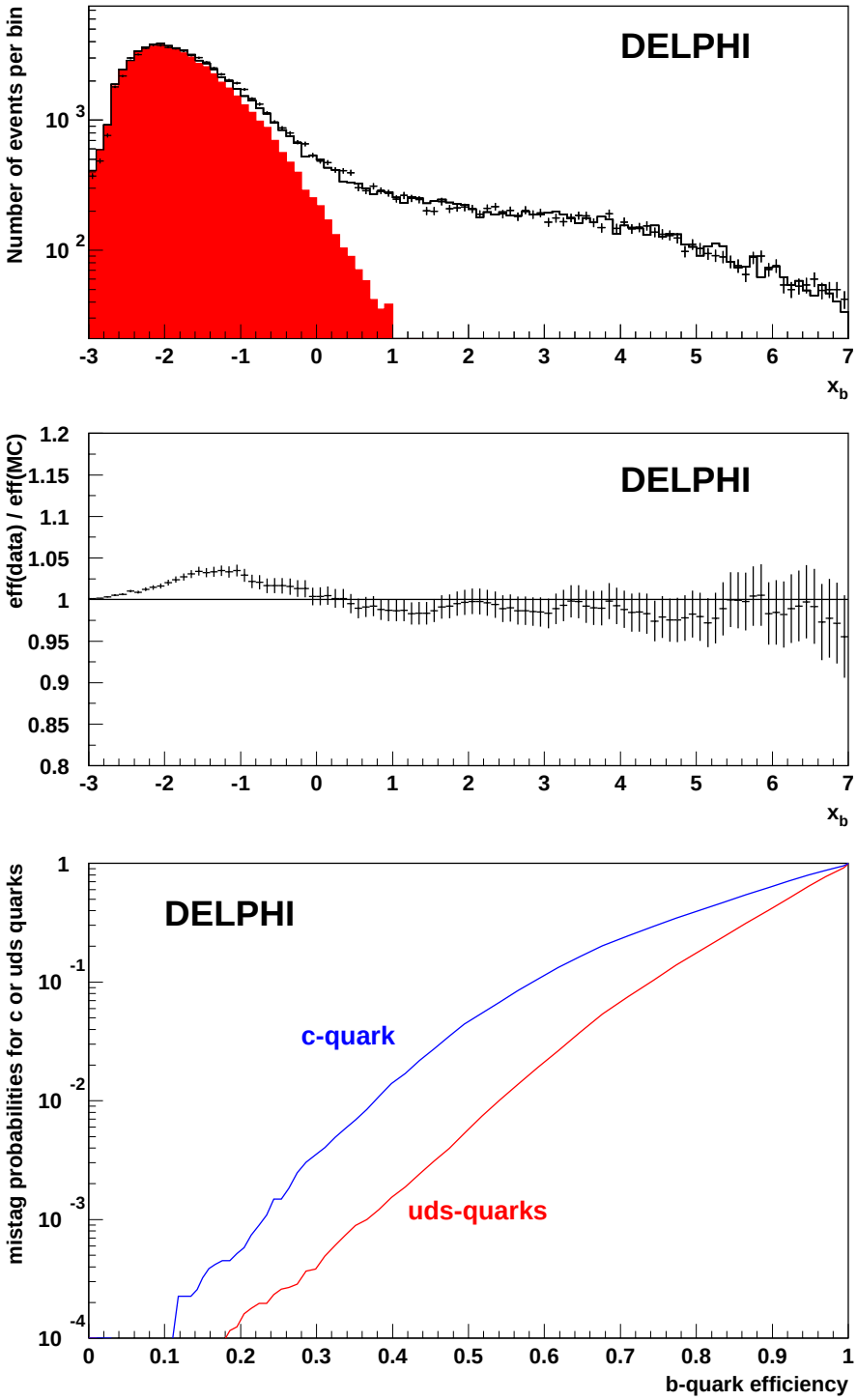

Figure 1: b-tagging: Top: distributions of the combined b-tagging variable x_{b}, in 1999 Z data (dots) and simulation (histogram). The contribution of udsc-quarks is shown as the dark histogram. Middle: ratio of integrated tagging rates in Z data and simulation as a function of the cut in x_{b}. Bottom: mistag probabilities for c or uds-quarks as a function of the efficiency for b-quarks, estimated from simulated Z data.

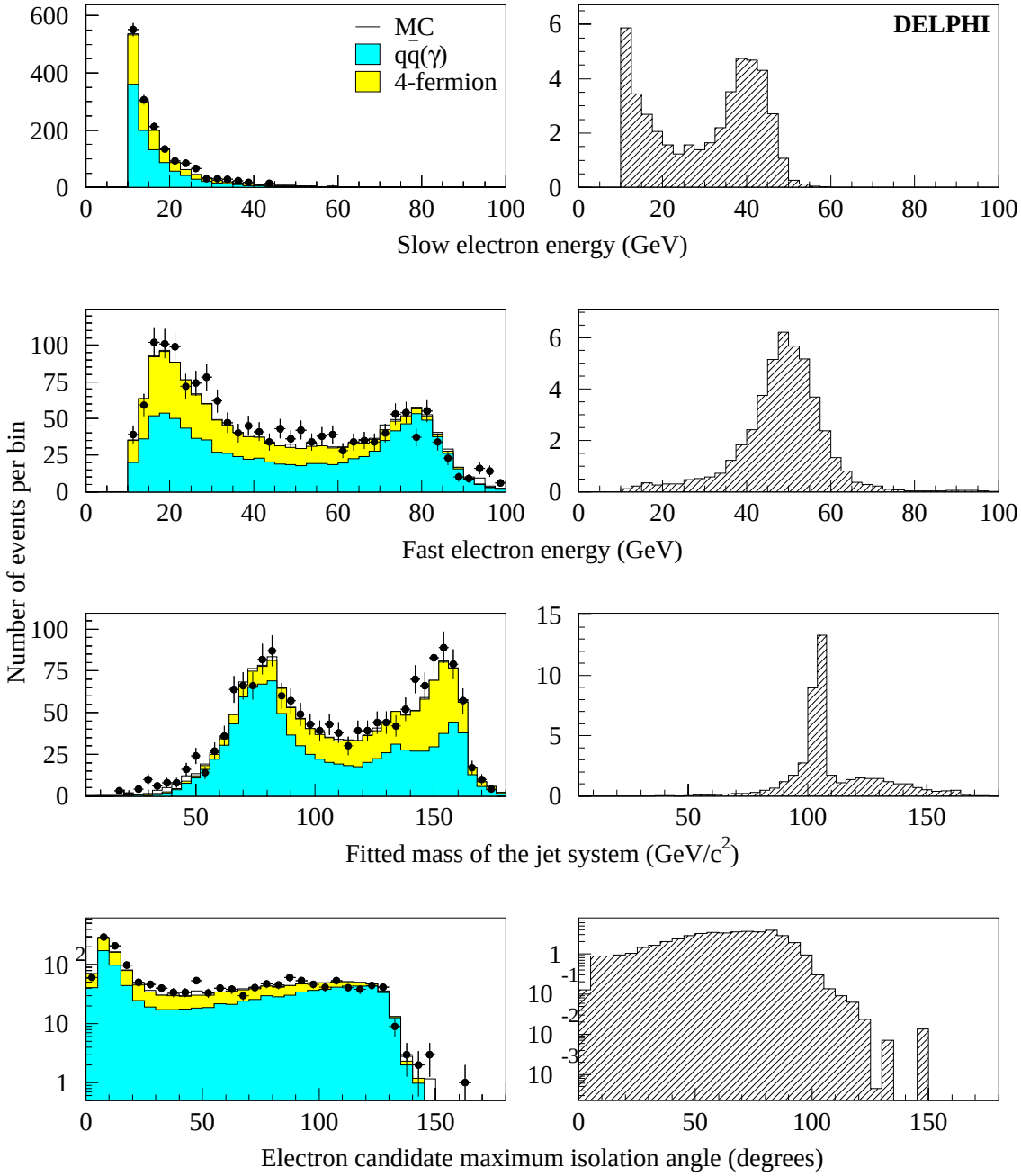

Figure 2: He^+e^-channel: distributions of four analysis variables, as described in the text, at preselection level. Data at $\sqrt{s}$ = 191.6-201.7 GeV (dots) are compared with SM background expectations (left-hand side histograms) and with the expected distribution for a 105 GeV/c^2 signal (right-hand side histogram, normalised to 50 times the expected rate).

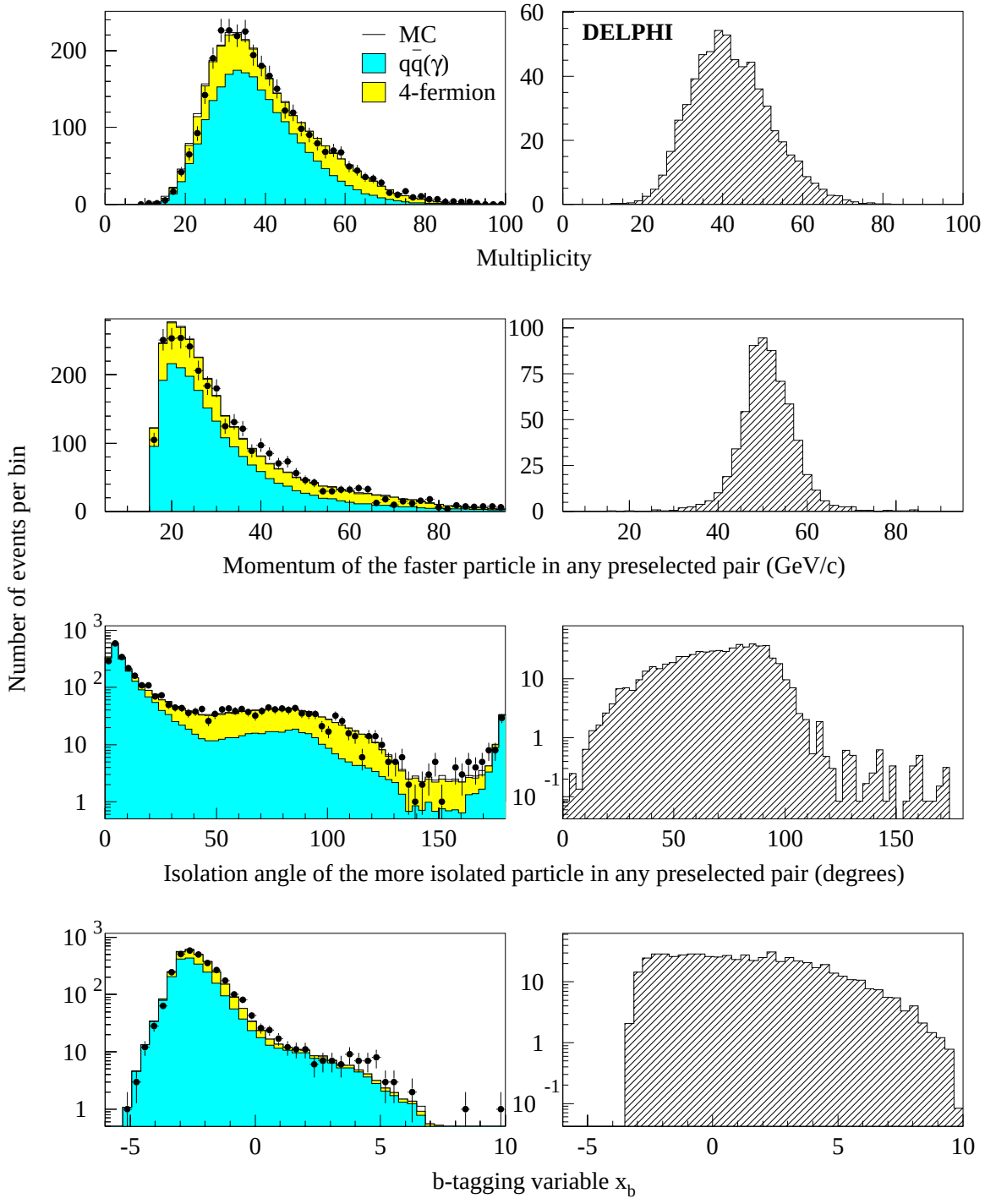

Figure 3: H$\mu^+\mu^-$ channel: distributions of four analysis variables, as described in the text, at preselection level. Data at $\sqrt{s}$ = 191.6-201.7 GeV (dots) are compared with SM background expectations (left-hand side histograms) and with the expected distribution for a 105 GeV/c^2 signal (right-hand side histogram, normalised to one thousand times the expected rate).

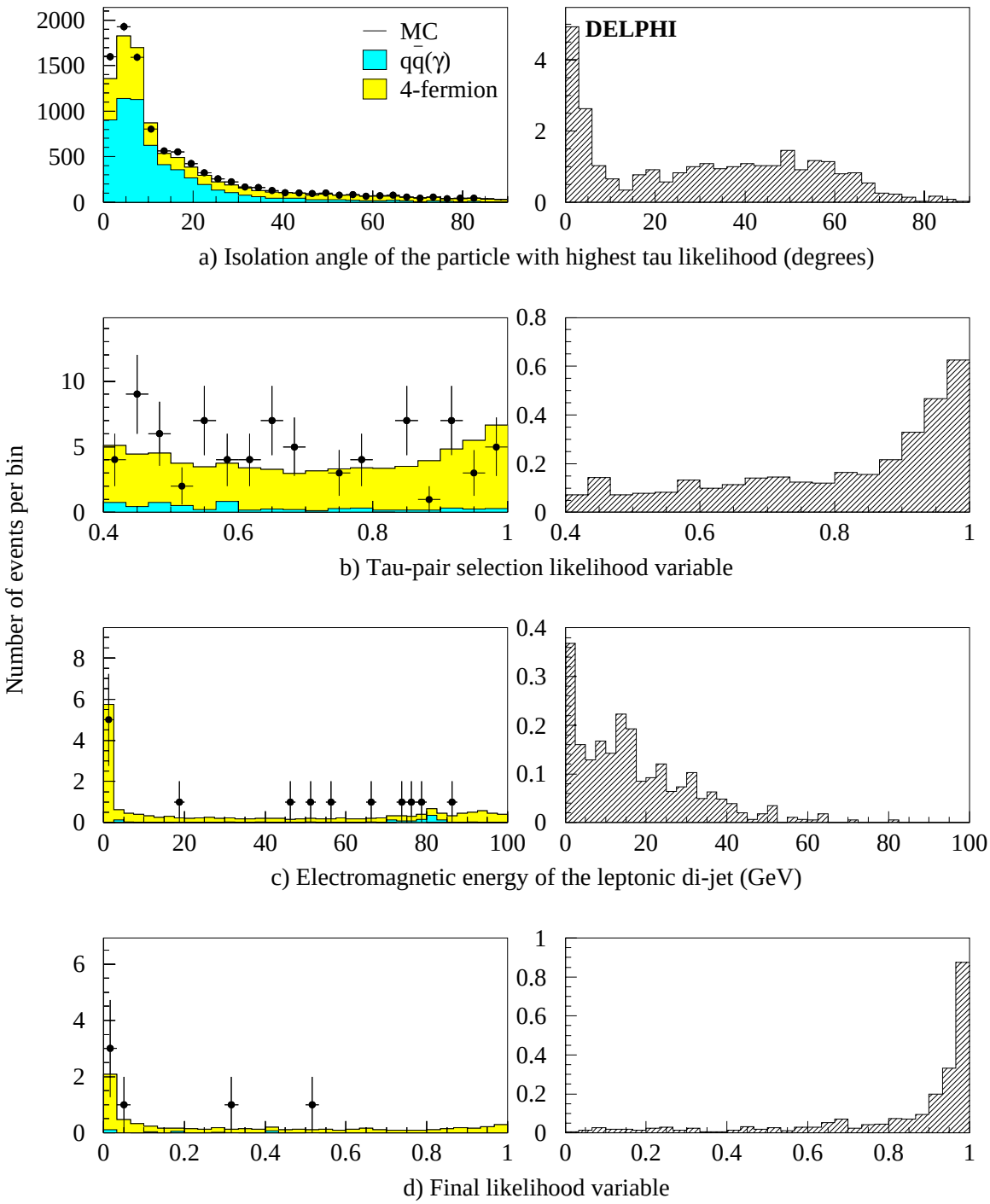

Figure 4: $\tau^+\tau^-\mathrm{q\bar{q}}$ channel: distributions of four analysis variables at different levels of the selection, as described in the text. Data at $\sqrt{s}$ = 191.6-201.7 GeV (dots) are compared with SM background expectations (left-hand side histograms) and with the expected distribution for a 105 GeV/c^2 signal in the (h$\rightarrow\tau^+\tau^-$)(Z$\rightarrow\mathrm{q\bar{q}}$) (right-hand side histogram, normalised to one hundred times the expected rate).

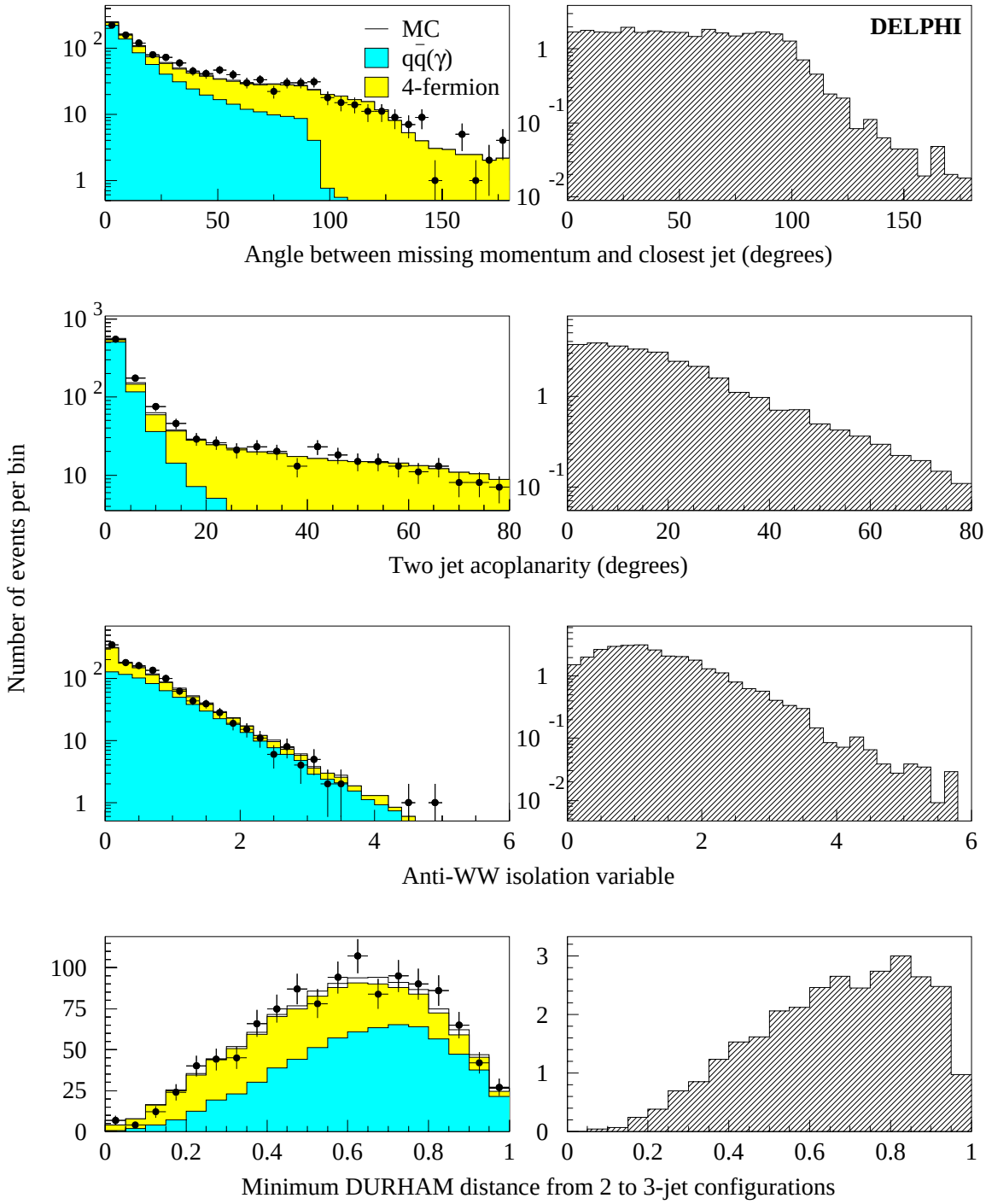

Figure 5: H$\nu\bar{\nu}$ channel: distributions of four analysis variables, as described in the text, at preselection level. Data at $\sqrt{s}$ = 191.6-201.7 GeV (dots) are compared with SM background expectations (left-hand side histograms) and with the expected distribution for a 105 GeV/c^2 signal (right-hand side histogram, normalised to 10 times the expected rate).

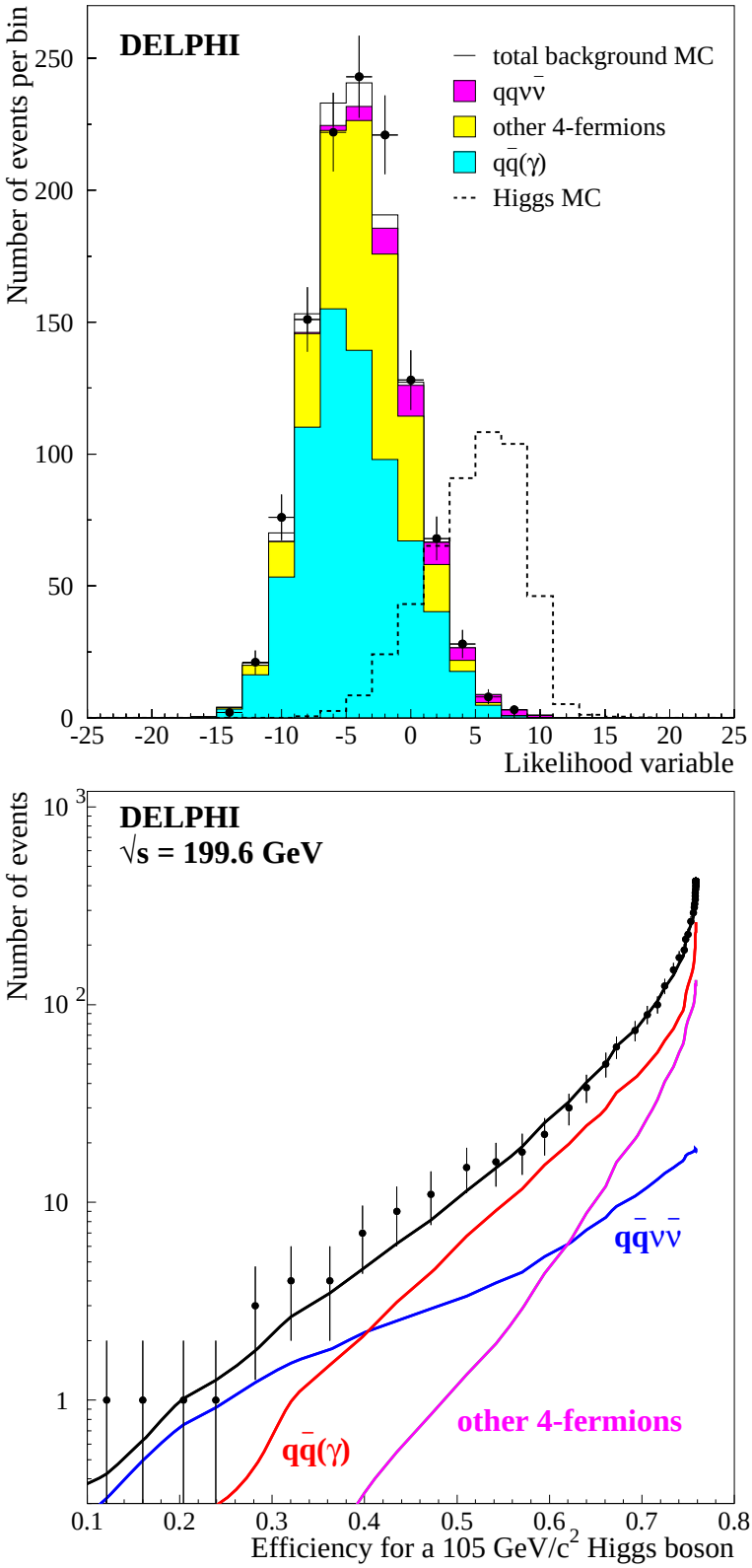

Figure 6: H$\nu\bar{\nu}$ channel: Top: distributions of the likelihood variable for the expected SM backgrounds (full histograms), 191.6-201.7 GeV data (dots) and the expected Higgs signal at 105 GeV/c^2 (dashed histogram, normalised to 100 times the expected rate). Bottom: curve of the expected SM background rate at $\sqrt{s}$ = 199.6 GeV as a function of the efficiency for a 105 GeV/c^2 Higgs signal when varying the cut on the likelihood variable. The different background contributions are shown separately. The dots represent the data.

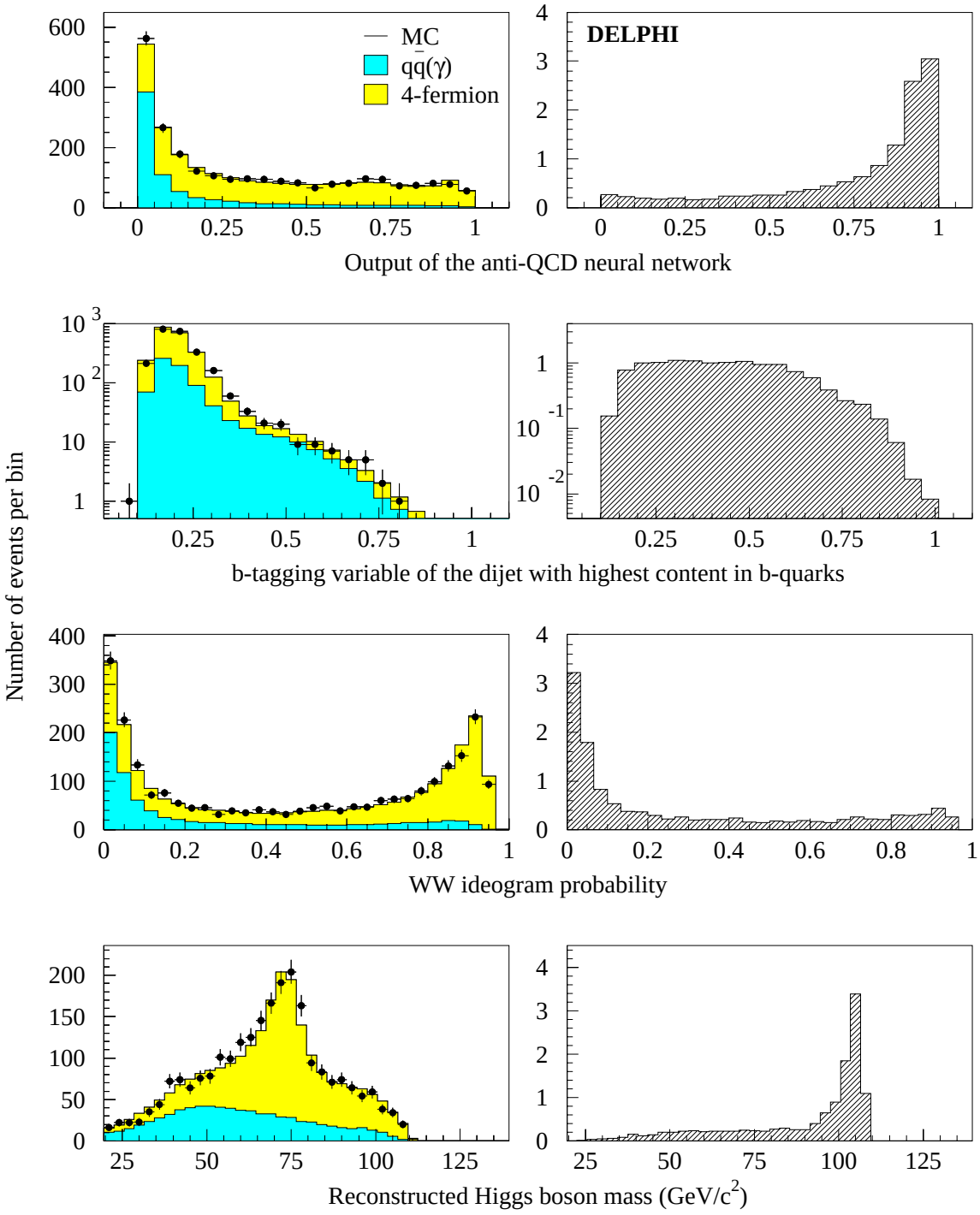

Figure 7: Hq$\bar{\text{q}}$ channel: distributions of four analysis variables, as described in the text, at preselection level. Data at $\sqrt{s}$ = 191.6-201.7 GeV (dots) are compared with SM background expectations (left-hand side histograms) and with the expected distribution for a 105 GeV/c^2 signal (right-hand side histogram, normalised to the expected rate).

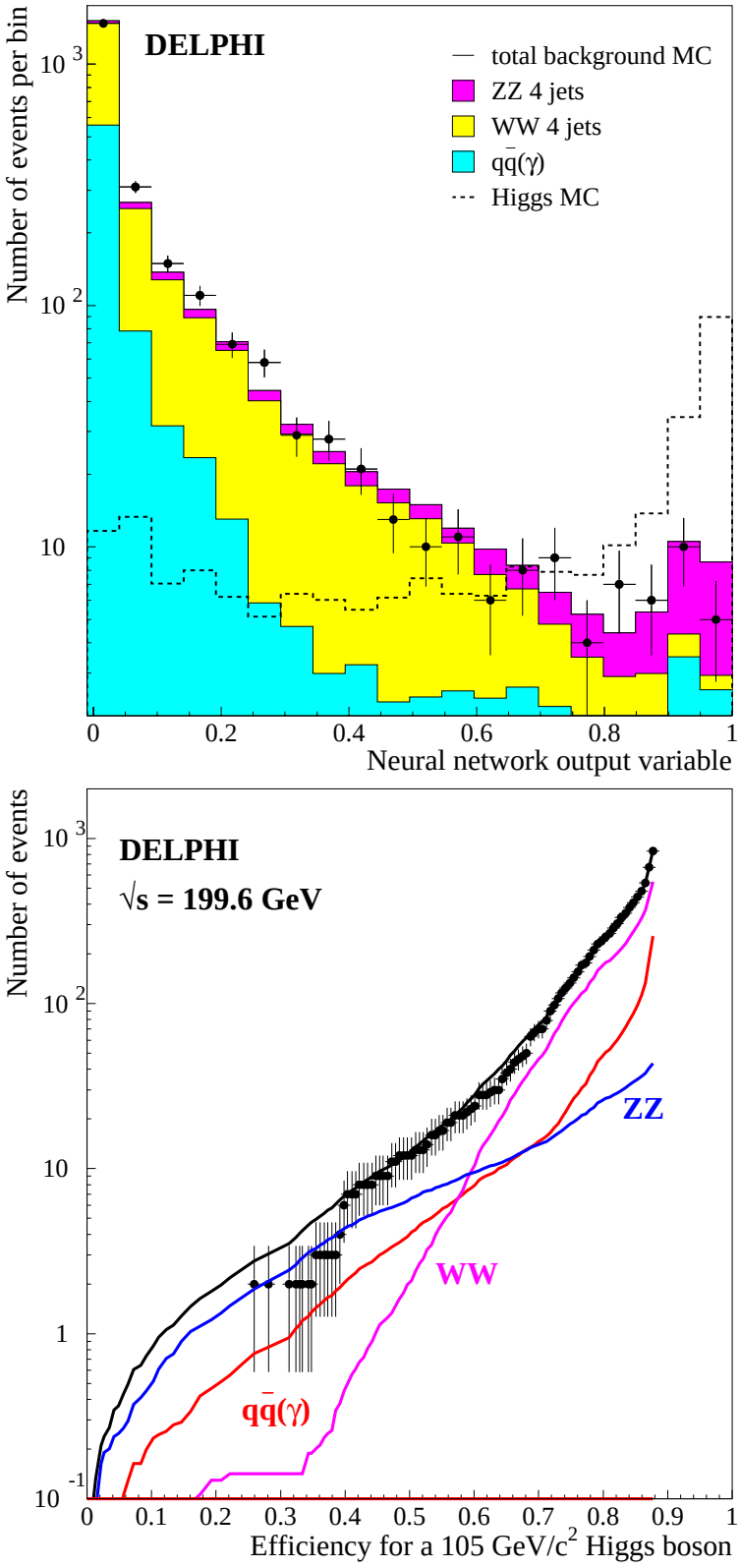

Figure 8: Hq$\bar{\text{q}}$ channel: Top: distributions of the neural network variable for the expected SM backgrounds (full histograms), 191.6-201.7 GeV data (dots) and the expected Higgs signal at 105 GeV/c^2 (dashed histogram, normalised to 20 times the expected rate). Bottom: curve of the expected SM background rate at $\sqrt{s} = 199.6$ GeV as a function of the efficiency for a 105 GeV/c^2 Higgs signal when varying the cut on the neural network variable. The different background contributions are shown separately. The dots represent the data.

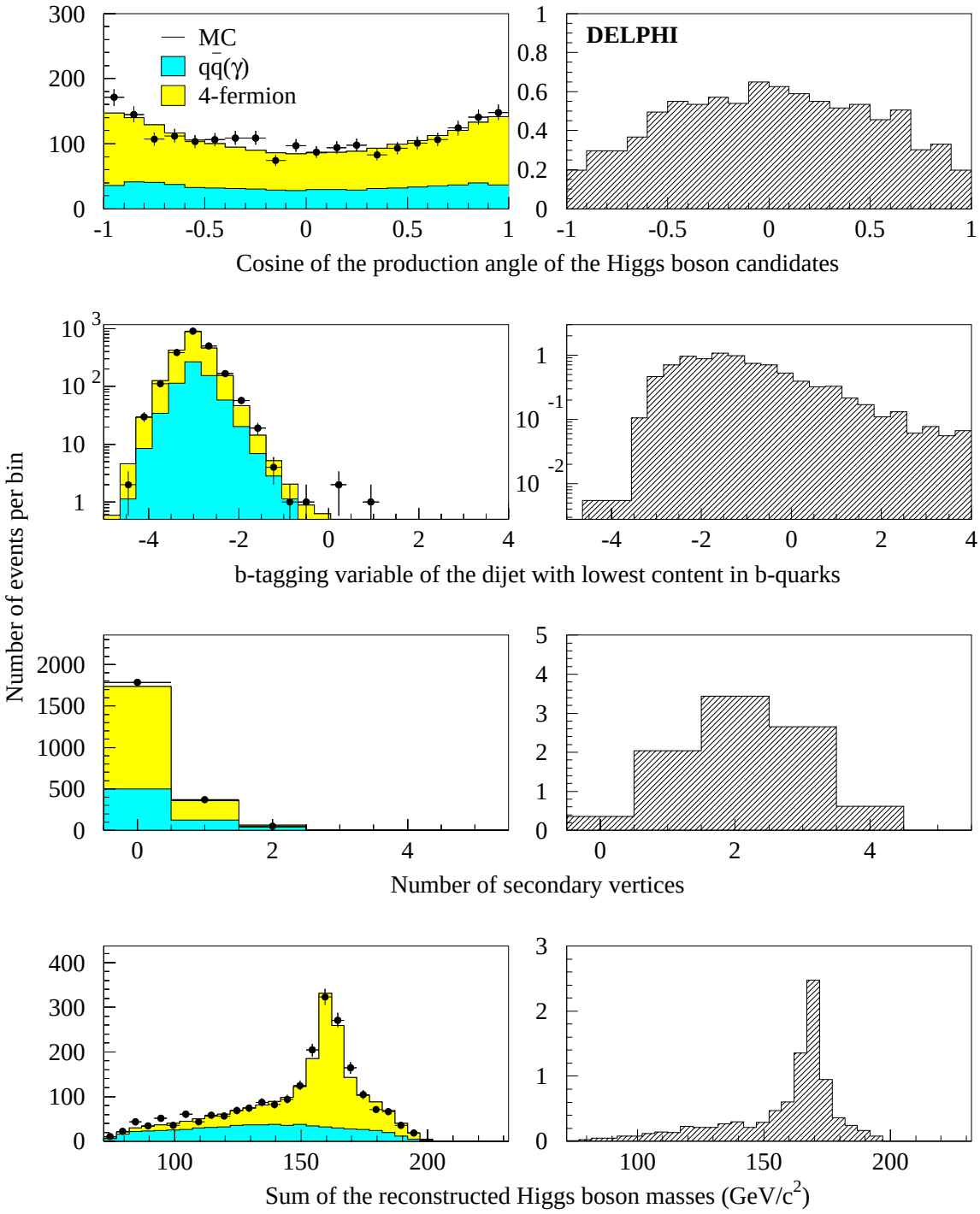

Figure 9: hA hadronic channel: distributions of four analysis variables, as described in the text, at preselection level. Data at $\sqrt{s}$ = 191.6-201.7 GeV (dots) are compared with SM background expectations (left-hand side histograms) and with the expected distribution for a 85 GeV/c^2 signal at $\tan\beta = 20$ (right-hand side histogram, normalised to the expected rate).

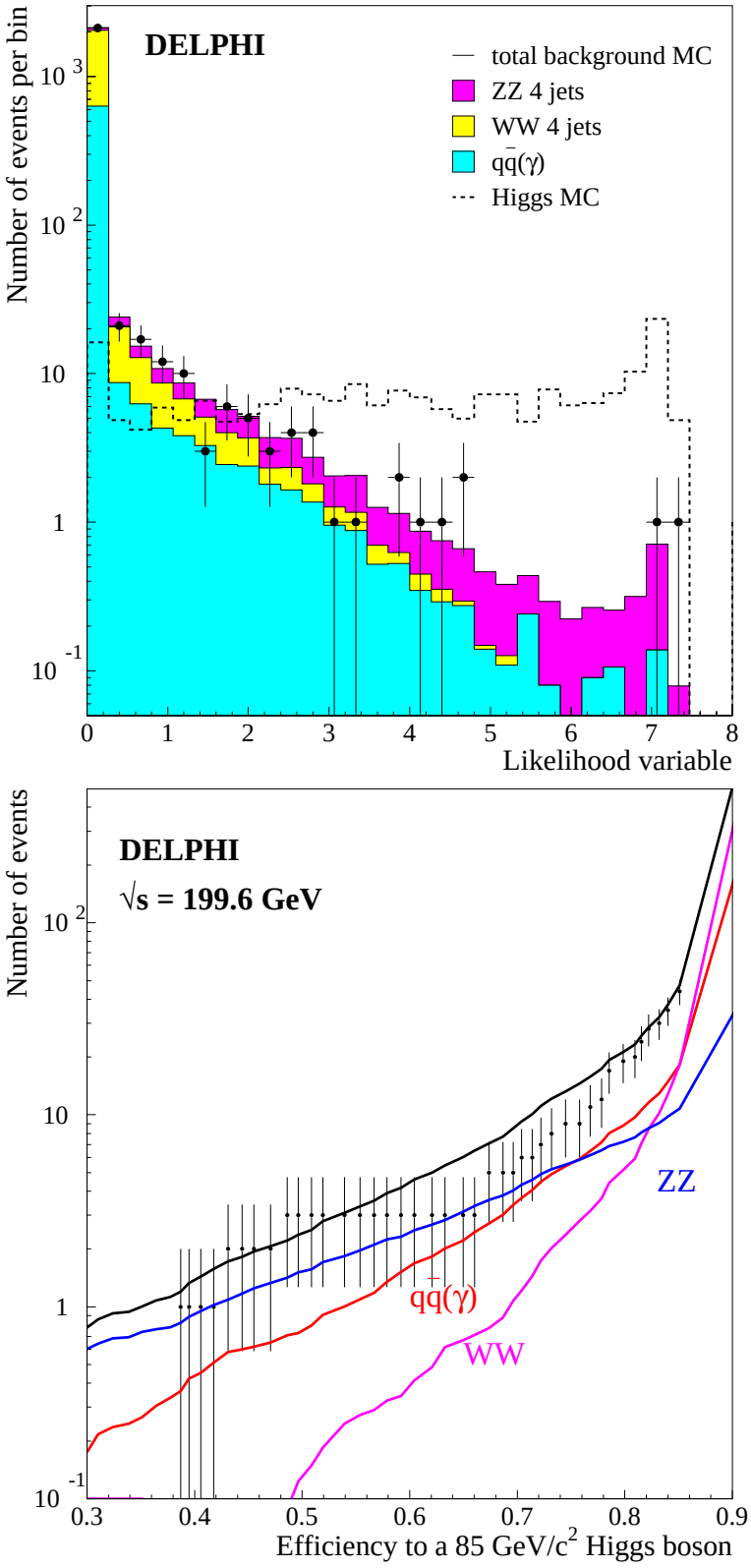

Figure 10: hA hadronic channel: Top: distributions of the likelihood variable for the expected SM backgrounds (full histograms), 191.6-201.7 GeV data (dots) and the expected 85 GeV/c^2 Higgs signal at $\tan\beta = 20$ (dashed histogram, normalised to 20 times the expected rate). Bottom: curve of the expected SM background rate at $\sqrt{s} = 199.6$ GeV as a function of the efficiency for a 85 GeV/c^2 Higgs signal at $\tan\beta = 20$ when varying the cut on the likelihood variable. The different background contributions are shown separately. The dots show the data.

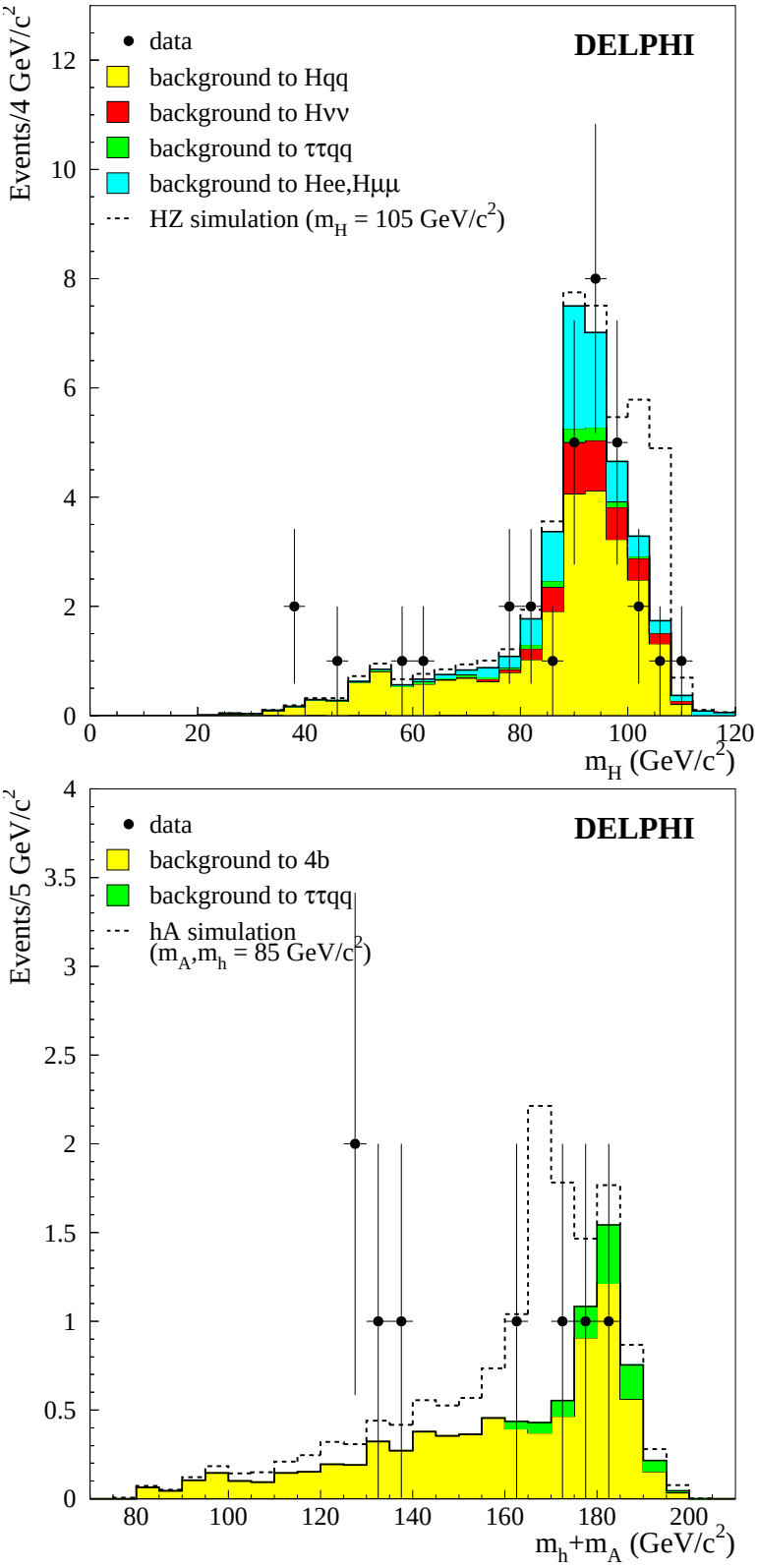

Figure 11: Distribution of the reconstructed Higgs boson mass(es) when combining all HZ or hA analyses at 191.6-201.7 GeV. Data (dots) are compared with SM background expectations (full histograms) and with the normalised signal spectrum added to the background contributions (dashed histogram). Mass hypotheses for the simulated signal spectra are $m_{\mathrm{H}} = 105$ GeV/c^2 in the HZ channel and $m_{\mathrm{A}} = 85$ GeV/c^2, $\tan\beta = 20$ in the hA channel.

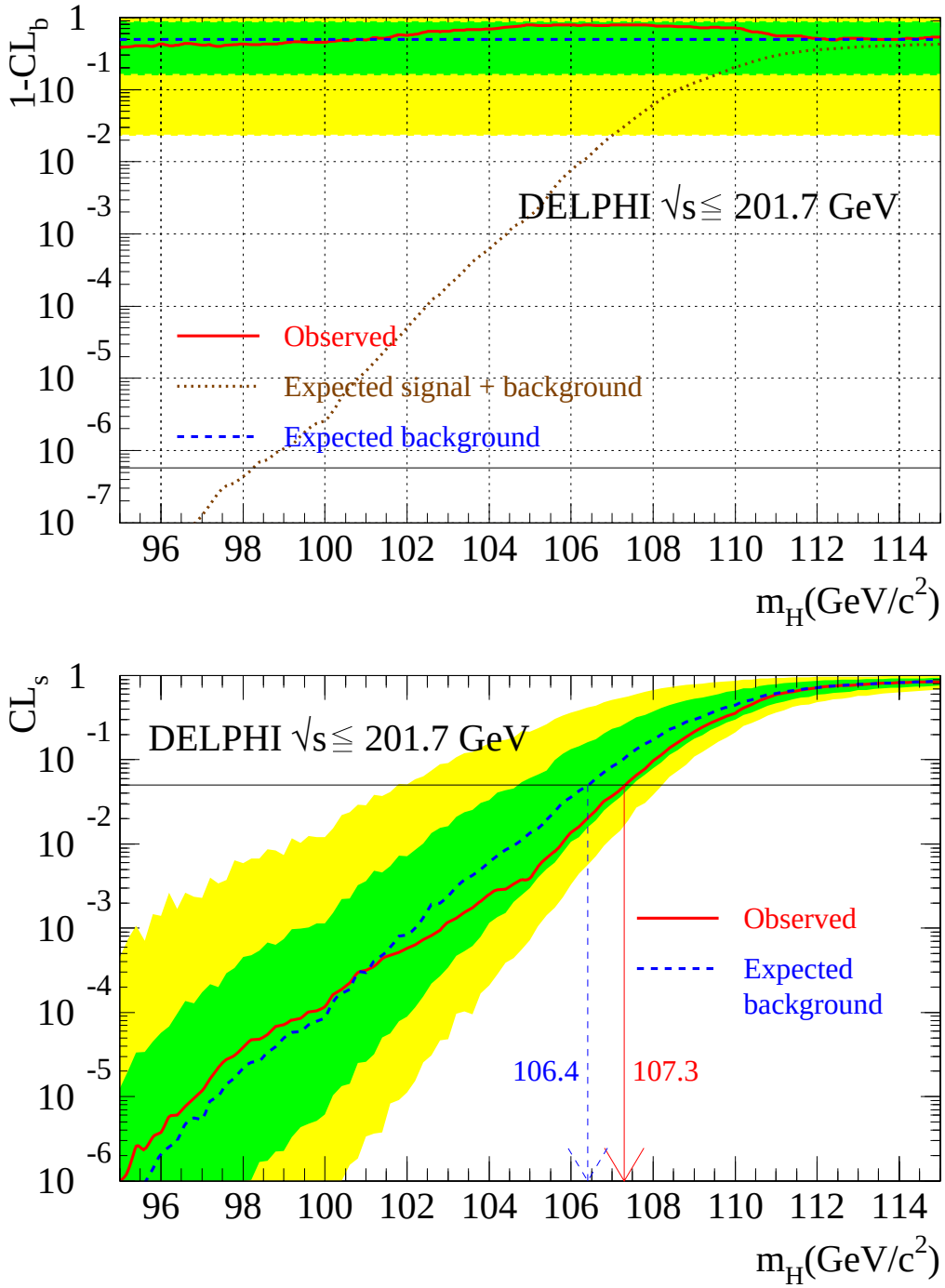

Figure 12: SM Higgs boson: confidence levels as a function of m_{H}. Curves are the observed (solid) and expected median (dashed) confidences from background-only experiments while the bands correspond to the 68.3% and 95.0% confidence intervals from background-only experiments. Top: 1- $\mathrm{CL_b}$ for the background hypothesis. Also shown here is the curve of the median confidence as expected for a signal of mass given in the abscissa (dotted line). The sensitivity for a 5σ discovery, defined by the horizontal line at 5.7 10^{-7}, is for Higgs masses up to 98.2 GeV/c^2. Bottom: $\mathrm{CL_s}$, the pseudo-confidence level for the signal hypothesis. The intersections of the curves with the horizontal line at 5% define the expected and observed 95% CL lower limits on m_{H}.

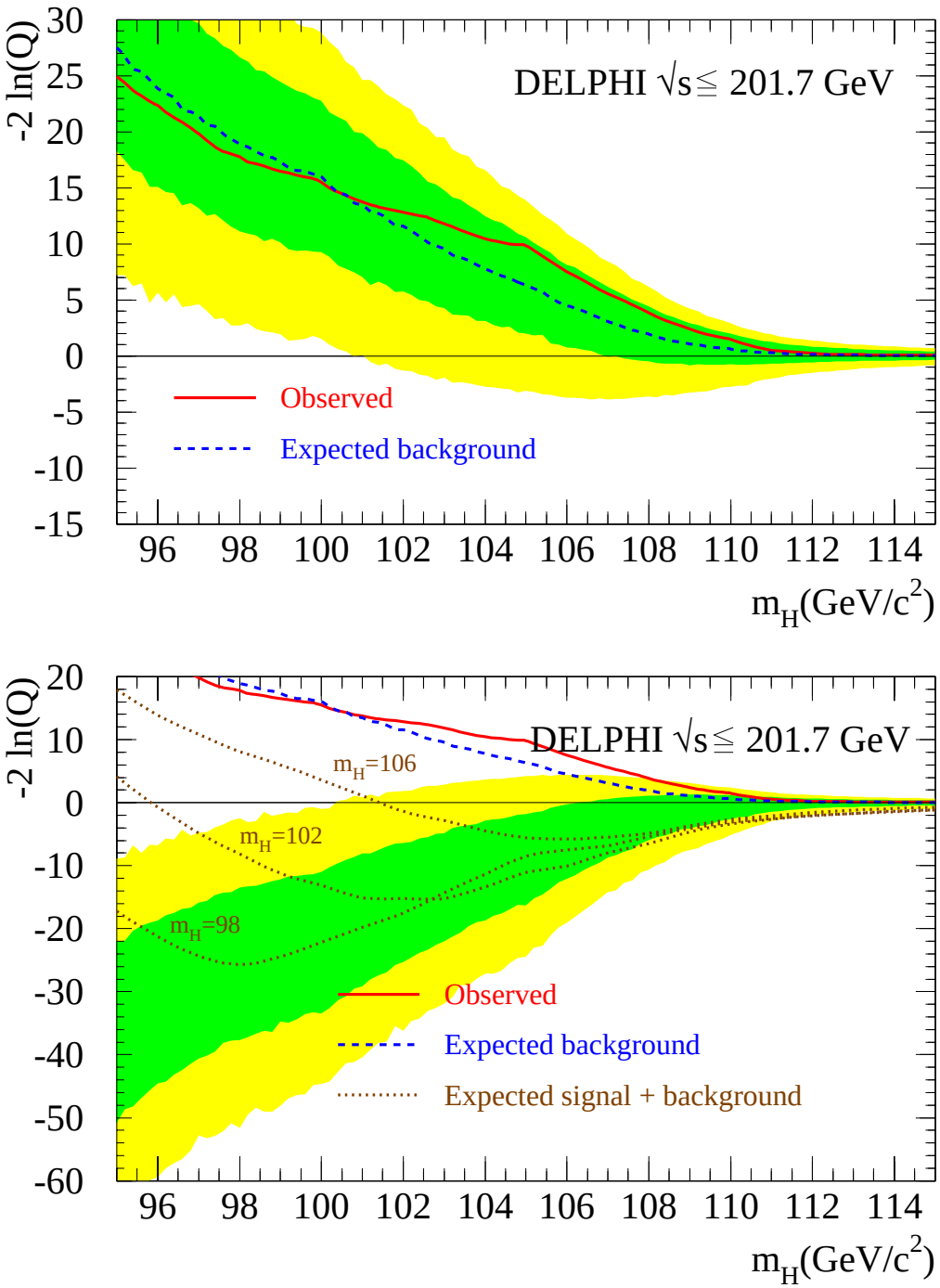

Figure 13: SM Higgs boson: test-statistic $\mathcal{Q}$ for each $m_{\rm H}$ hypothesis in data (solid) and its expected median value in background-only experiments (dashed). Top: the bands correspond to the 68.3% and 95.0% confidence intervals from background-only experiments. Bottom: the bands represent the confidence intervals around the minima of the $-2ln\mathcal{Q}$ curves expected for a signal of mass given in the abscissa while the dotted lines show the median curves expected for three mass hypotheses.

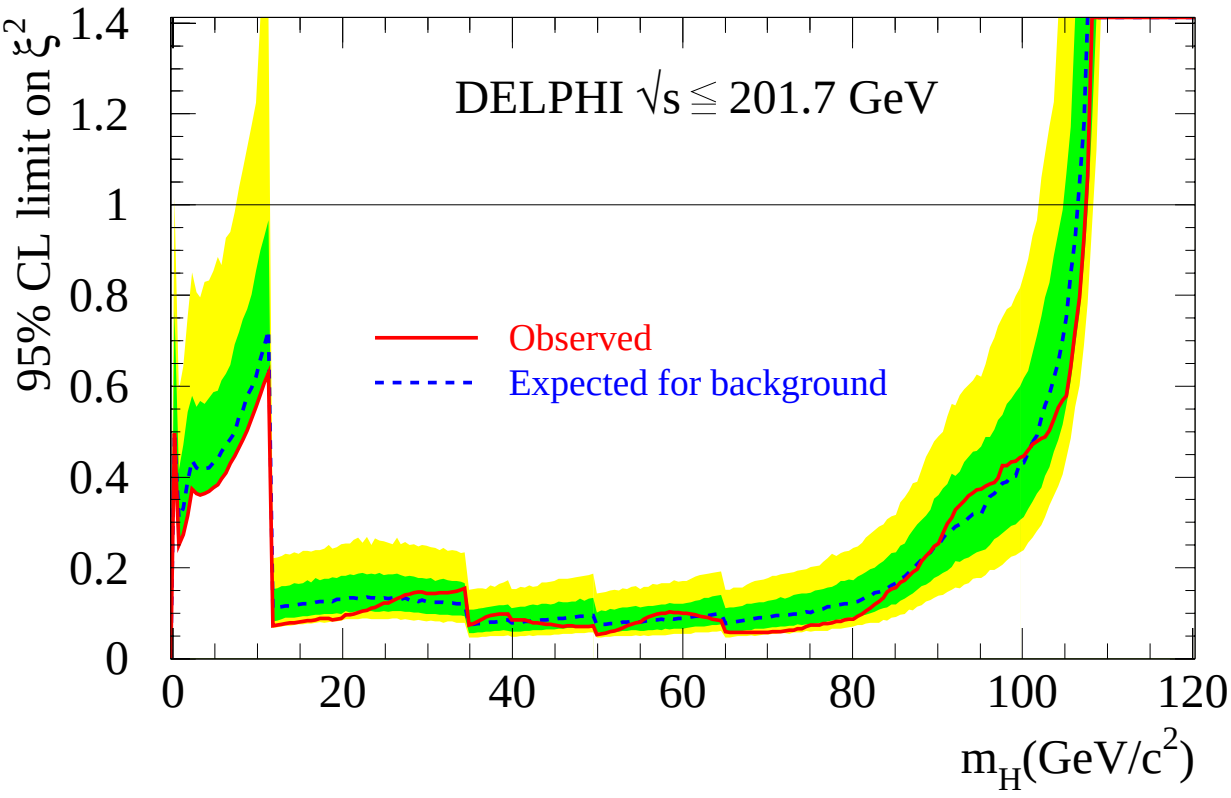

Figure 14: 95% CL upper bound on ξ^2, where ξ is the HVV (V=W$^{\pm}$ or Z) coupling normalised to that in the SM, assuming SM branching fractions for the Higgs boson. The limit observed in data (solid line) is shown together with the expected median limit in background-only experiments (dashed line). The bands correspond to the 68.3% and 95.0% confidence intervals from background-only experiments. Most of the jumps below 40 GeV/c^2 correspond to the different analyses applied to different subsets of LEP1 data to cover the various topologies expected from a Higgs boson. The jumps at 12, 50 and 65 GeV/c^2 indicate where the LEP2 results at 191.6-201.7, 182.7 and 188.7 GeV/c^2 respectively start to contribute.

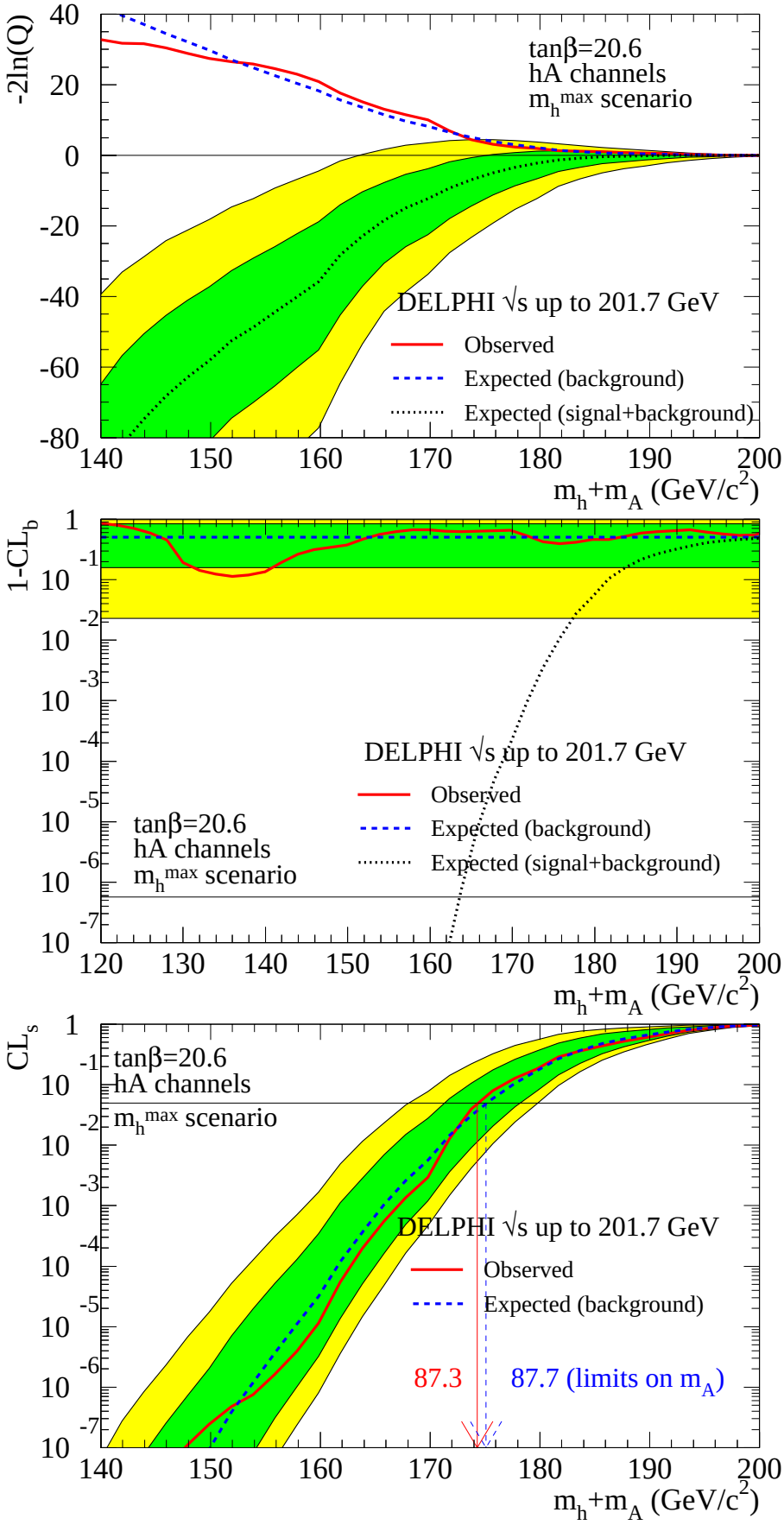

Figure 15: hA analyses: test-statistic (top) and confidence levels in background hypothesis (middle) and in signal hypothesis (bottom) as functions of $m_{\mathrm{h}}+m_{\mathrm{A}}$. Curves are the observed (solid) and median expected (dashed) confidences from background-only experiments while the bands correspond to the 68.3% and 95.0% confidence intervals from background+signal experiments for a signal of mass given in the abscissa (top) and from background-only experiments (middle and bottom).

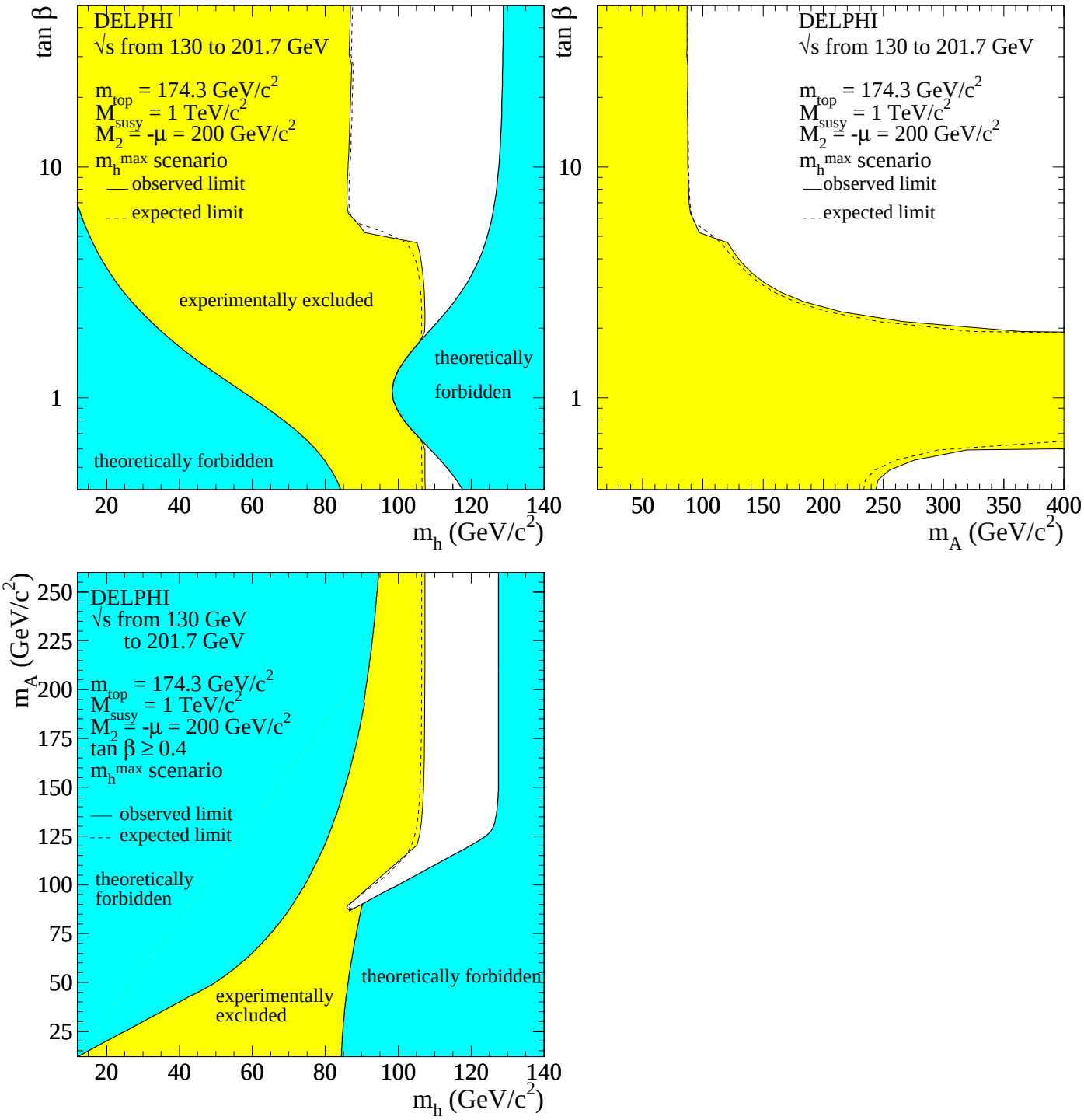

Figure 16: MSSM Higgs bosons: regions excluded at 95% CL by the searches in the hZ and hA channels up to $\sqrt{s} = 201.7$ GeV, in the m_h^{max} scenario. The dark shaded areas are the regions not allowed by the MSSM model in this scenario. The dashed lines show the median expected limits.

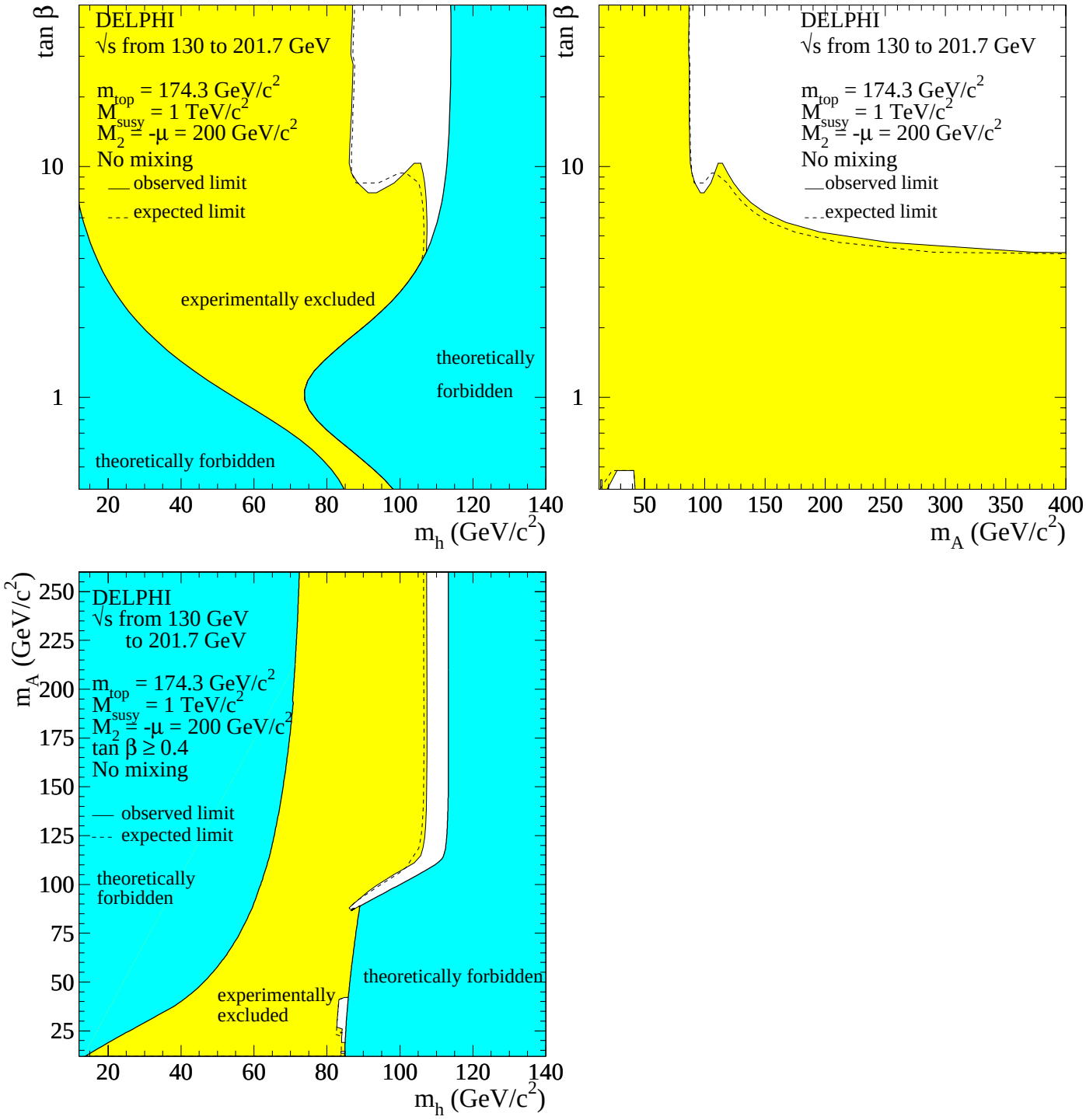

Figure 17: MSSM Higgs bosons: regions excluded at 95% CL by the searches in the hZ and hA channels up to $\sqrt{s} = 201.7$ GeV, in the no mixing scenario. There is a region at m_{h} around of 85 GeV/c^2 and small $\tan\beta$ that is not excluded, but is too small to be visible in the top left-hand plot. The dark shaded areas are the regions not allowed by the MSSM model in this scenario. The dashed lines show the median expected limits.

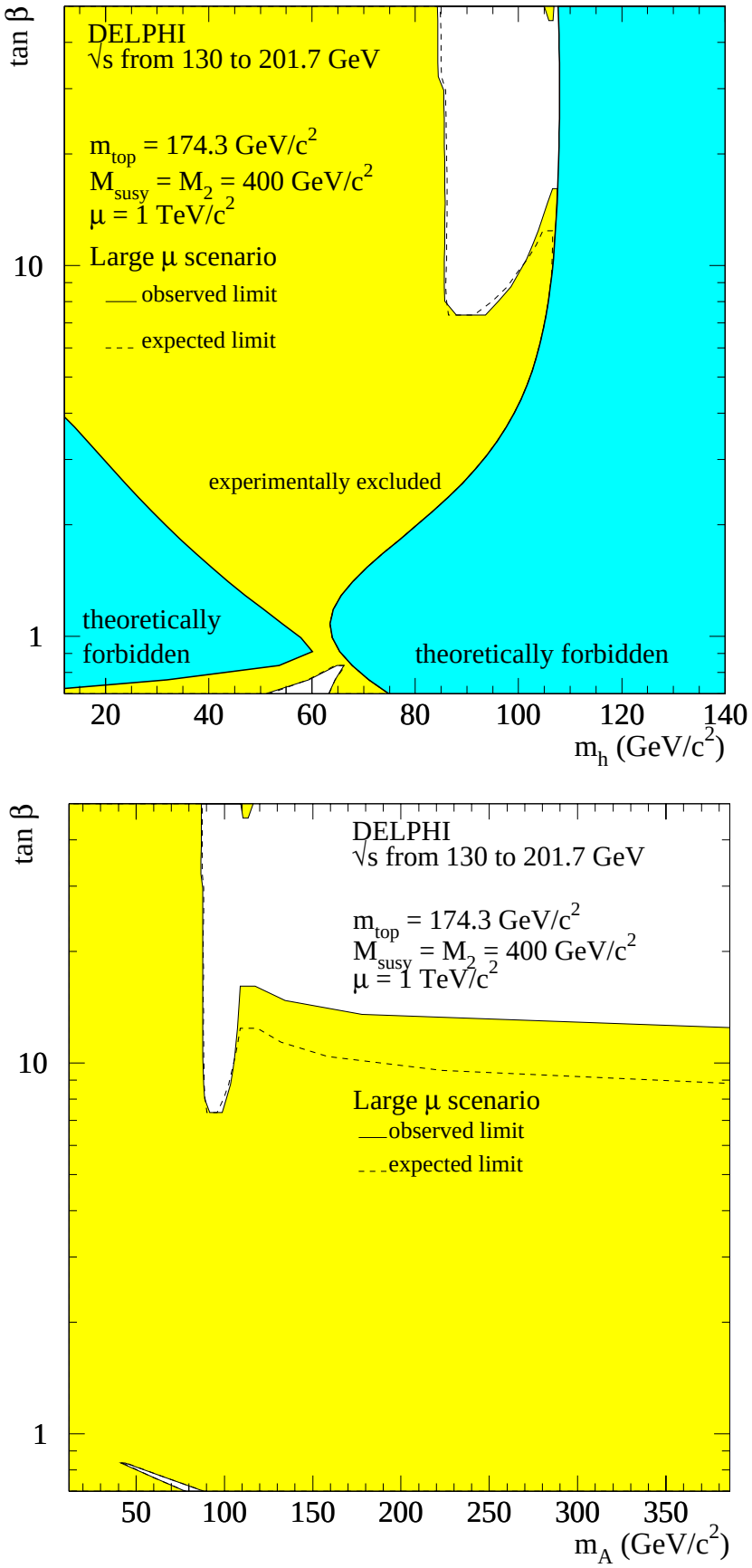

Figure 18: MSSM Higgs bosons: regions excluded at 95% CL, by the searches in the hZ and hA channels up to $\sqrt{s} = 201.7$ GeV, in the large μ scenario. The dark shaded areas are the regions not allowed by the MSSM model in this scenario. The dashed lines show the median expected limits.

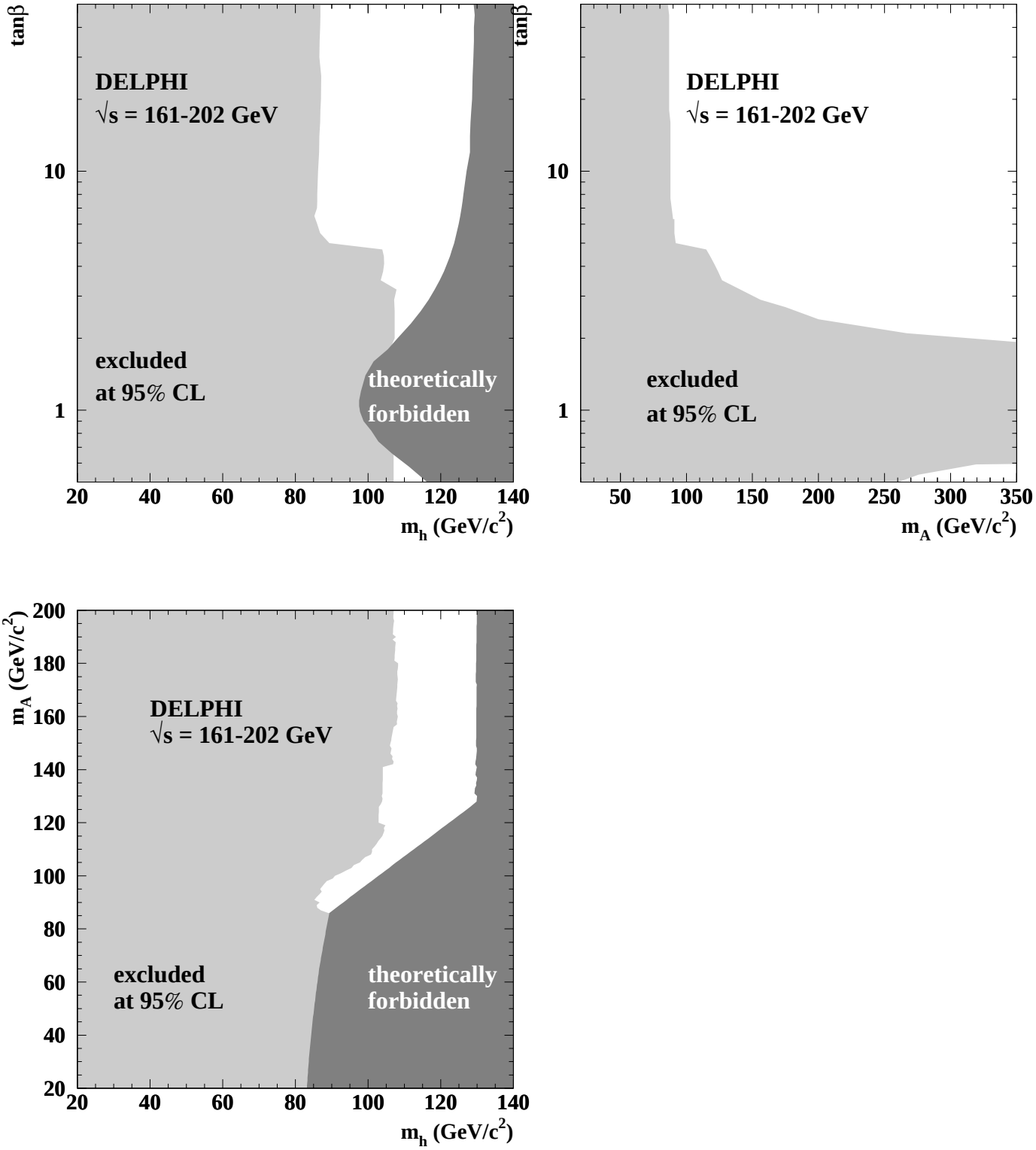

Figure 19: MSSM Higgs bosons: regions excluded at 95% CL by the searches in the hZ and hA channels up to $\sqrt{s} = 201.7$ GeV, in an extended scan of the MSSM parameter space. The dark shaded area is the region at high m_{h} not allowed by the MSSM model in this scan.